J. Phys. Chem. A **2007,** *111,* 9145−9163

DFT-Based Studies on the Jahn−Teller Effect in 3d Hexacyanometalates with Orbitally Degenerate Ground States

Mihial Atanasov,*,†,‡,§ Peter Comba,*,‡ Claude A. Daul,§ and Andreas Hauser‖

Institute of General and Inorganic Chemistry, Bulgarian Academy of Sciences, Acad. Georgi Bontchev Str. Bl.11, 1113 Sofia, Bulgaria, Anorganisch-Chemisches Institut, Universität Heidelberg, Im Neuenheimer Feld 270, D-69120 Heidelberg, Germany, Département de Chimie, Université de Fribourg, Ch. du Musée 9, CH-1700 Fribourg, Switzerland, and Département de Chimie Physique, Université de Genève, Genève, Switzerland

Received: April 25, 2007; In Final Form: June 25, 2007

The topology of the ground-state potential energy surface of $M(CN)_6$ with orbitally degenerate $^2T_{2g}$ (M = Ti^{III} ($t_{2g}{}^1$), Fe^{III} and Mn^{II} (both low-spin $t_{2g}{}^5$)) and $^3T_{1g}$ ground states (M = V^{III} ($t_{2g}{}^2$), Mn^{III} and Cr^{II} (both low-spin $t_{2g}{}^4$)) has been studied with linear and quadratic Jahn−Teller coupling models in the five-dimensional space of the ϵ_g and τ_{2g} octahedral vibrations ($T_g\otimes(\epsilon_g+\tau_{2g})$ Jahn−Teller coupling problem ($T_g = {}^2T_{2g}, {}^3T_{1g}$)). A procedure is proposed to give access to all vibronic coupling parameters from geometry optimization with density functional theory (DFT) and the energies of a restricted number of Slater determinants, derived from electron replacements within the $t_{2g}{}^{1,5}$ or $t_{2g}{}^{2,4}$ ground-state electronic configurations. The results show that coupling to the τ_{2g} bending mode is dominant and leads to a stabilization of D_{3d} structures (absolute minima on the ground-state potential energy surface) for all complexes considered, except for $[Ti(CN)_6]^{3-}$, where the minimum is of D_{4h} symmetry. The Jahn−Teller stabilization energies for the D_{3d} minima are found to increase in the order of increasing CN−M π back-donation ($Ti^{III} < V^{III} < Mn^{III} < Fe^{III} < Mn^{II} < Cr^{II}$). With the angular overlap model and bonding parameters derived from angular distortions, which correspond to the stable D_{3d} minima, the effect of configuration interaction and spin−orbit coupling on the ground-state potential energy surface is explored. This approach is used to correlate Jahn−Teller distortion parameters with structures from X-ray diffraction data. Jahn−Teller coupling to trigonal modes is also used to reinterpret the anisotropy of magnetic susceptibilities and **g** tensors of $[Fe(CN)_6]^{3-}$, and the $^3T_{1g}$ ground-state splitting of $[Mn(CN)_6]^{3-}$, deduced from near-IR spectra. The implications of the pseudo Jahn−Teller coupling due to t_{2g}−e_g orbital mixing via the trigonal modes (τ_{2g}) and the effect of the dynamic Jahn−Teller coupling on the magnetic susceptibilities and **g** tensors of $[Fe(CN)_6]^{3-}$ are also addressed.

I. Introduction

Hexacynometalates of 3d metal ions are characterized by $t_{2g}{}^n$ electronic configurations and orbitally degenerate low-spin ground states: $^3T_{1g}$ for Mn^{III} and Cr^{II} (d^4) and $^2T_{2g}$ for Fe^{III} and Mn^{II} (d^5). These systems as well as Ti^{III} ($^2T_{2g}$, d^1) and V^{III} ($^3T_{1g}$, d^2) are Jahn−Teller (JT) active.[1,2] The ϵ_g and τ_{2g} octahedral vibrational modes lift the orbital degeneracy and lower the energy of the system ($T_g\otimes(\epsilon_g+\tau_{2g})$ JT coupling, $T_g = {}^2T_{2g}, {}^3T_{1g}$). JT and vibronic couplings have usually been ignored in theoretical studies of the magnetic properties of room-temperature magnets, derived from Prussian blue analogues with $M(CN)_6$ as building blocks for oligonuclear complexes.[3,4] $T_g\otimes(\epsilon_g+\tau_{2g})$ JT coupling in complexes with π-bonding or -antibonding T_g states is expected to be weaker than that in systems where d electrons occupy the σ-antibonding e_g subshell ($E\otimes\epsilon_g$ JT coupling). A prominent example is that of complexes of Cu^{II}.[5−7] However, energies involved in the $T_g\otimes(\epsilon_g+\tau_{2g})$ JT interaction are comparable to spin−orbit coupling energies and, therefore, are expected to strongly modify the magnetic behavior.

$T_g\otimes(\epsilon_g+\tau_{2g})$ JT coupling in octahedral complexes has been treated in the limiting case of linear and the more thorough case of quadratic JT coupling.[8−10] A typical problem with these models is the large number of symmetry-independent parameters, which usually are larger than the number of observables (four harmonic force and vibronic coupling constants for linear and eight for quadratic JT coupling models). We have applied density functional theory (DFT) to the $T_g\otimes\epsilon_g$ problem in $M(CN)_6$ complexes (M = Ti^{III}, V^{III}, Mn^{III}, Fe^{III}, Cr^{II}, Mn^{II}).[11] DFT is used to deduce vibronic coupling parameters, which then are used for the calculation of structural distortions and JT stabilization energies.[11] Here, we give an extension of this DFT-based approach, which allows us to consider all five ϵ_g and τ_{2g} vibrations and to explore the topology of the ground-state potential energy surface. The $T_g\otimes(\epsilon_g+\tau_{2g})$ problem in octahedral T_g ground states is isomorphic with the $T\otimes(\epsilon+\tau_2)$ problem in tetrahedral complexes of Cu^{II} ($^2T_2$) and Ni^{II} ($^3T_1$). In a study on the symmetry aspects of the JT effect in these systems, group theoretical concepts were applied to describe the lowest and intermediate subgroups, starting from the high-symmetry (cubic) reference configuration.[12] With symmetry concepts we are able to simplify the $T_g\otimes(\epsilon_g+\tau_{2g})$ multimode JT problem.

---

* To whom correspondence should be addressed at Universität Heidelberg. Fax: (+49) 6221-546617. E-mail: peter.comba@aci.uni-heidelberg.de (P.C.); mihail.atanasov@aci.uni-heidelberg.de (M.A.).

† Bulgarian Academy of Sciences.

‡ Universität Heidelberg.

§ Université de Fribourg.

‖ Université de Genève.

10.1021/jp0731912 CCC: \$37.00

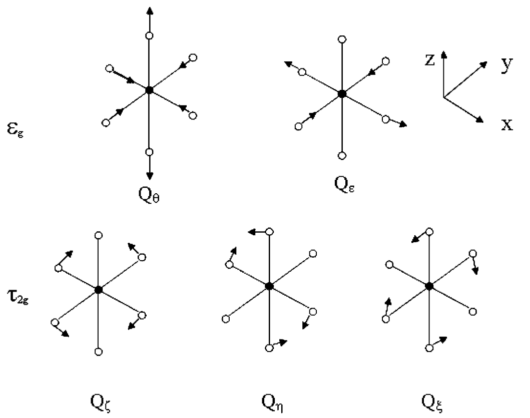

Figure 1. Components and shapes of the ϵ_g and τ_g octahedral vibrations.

Our aim is to calculate all stationary points (energy minima and saddle points) on the ground-state potential energy surface in $M(CN)_6$ ($M = Ti^{III}, V^{III}, Mn^{III}, Fe^{III}, Cr^{II}, Mn^{II}$), on the basis of DFT and a $T_g\otimes(\epsilon_g+\tau_{2g})$ vibronic coupling model. While energy minima are expected to dominate the low-temperature magnetic behavior, saddle points (transition states) are important for the reactivity in these and other related systems. To check the theory, we have applied this approach to experimental data of $K_3[Fe(CN)_6]$ and $K_3[Mn(CN)_6]$, for which isotropic and anisotropic susceptibility data are available.[13−25] The ground-state splitting of $[Mn(CN)_6]^{3-}$, derived from high-resolution spectroscopy of $K_3[Mn(CN)_6]$, and **g** tensor data of $[Fe(CN)_6]^{3-}$ are also included in the analysis.[13] Implications of pseudo and dynamic JT coupling have been studied with $[Fe(CN)_6]^{3-}$ as a model complex.

II. Theory

a. Vibronic Coupling Model and Symmetry Analysis of the Topology of the $T_g\otimes(\epsilon_g+\tau_{2g})$ Ground-State Adiabatic Potential Energy Surface. The Hamiltonian matrix of the $T_g\otimes(\epsilon_g+\tau_{2g})$ vibronic coupling problem up to second-order vibronic coupling terms is given by[26,27]

$$\begin{aligned}\mathbf{H} = {} & \left[\frac{1}{2}K_\epsilon(Q_\theta^{\,2}+Q_\epsilon^{\,2})+\frac{1}{2}K_\tau(Q_\xi^{\,2}+Q_\eta^{\,2}+Q_\zeta^{\,2})\right]\mathbf{I} + \\ & \left[V_\epsilon Q_\theta+\frac{1}{2}L_\epsilon(Q_\epsilon^{\,2}-Q_\theta^{\,2})-\frac{1}{4}L_\tau(2Q_\zeta^{\,2}-Q_\xi^{\,2}-Q_\eta^{\,2})\right]\mathbf{C}_\theta + \\ & \left[V_\epsilon Q_\epsilon+L_\epsilon Q_\theta Q_\epsilon-\frac{\sqrt{3}}{4}L_\tau(Q_\xi^{\,2}-Q_\eta^{\,2})\right]\mathbf{C}_\epsilon+\Bigg[V_\tau Q_\xi + \\ & X_\tau Q_\eta Q_\zeta+W\left(-\frac{1}{2}Q_\theta+\frac{\sqrt{3}}{2}Q_\epsilon\right)Q_\xi\Bigg]\mathbf{C}_\xi+\Bigg[V_\tau Q_\eta + \\ & X_\tau Q_\xi Q_\zeta+W\left(-\frac{1}{2}Q_\theta-\frac{\sqrt{3}}{2}Q_\epsilon\right)Q_\eta\Bigg]\mathbf{C}_\eta + \\ & [V_\tau Q_\zeta+X_\tau Q_\xi Q_\eta+WQ_\zeta Q_\theta]\mathbf{C}_\zeta \qquad (1)\end{aligned}$$

Q_θ and Q_ϵ and Q_ξ, Q_η, and Q_ζ are the ϵ_g and τ_{2g} vibrations, respectively (see Figure 1). With Griffith's standard notation the basis of the matrix representation is $T_{1g}\alpha$, $T_{1g}\beta$, $T_{1g}\gamma$ or $T_{2g}\xi$, $T_{2g}\eta$, $T_{2g}\zeta$.[28] **I** is the (3 × 3) unit matrix. The **C** matrices with the appropriate coupling coefficients are defined as

$$\mathbf{C}_\theta = \begin{pmatrix} \frac{1}{2} & 0 & 0 \\ 0 & \frac{1}{2} & 0 \\ 0 & 0 & -1 \end{pmatrix}$$

$$\mathbf{C}_\epsilon = \begin{pmatrix} -\frac{\sqrt{3}}{2} & 0 & 0 \\ 0 & \frac{\sqrt{3}}{2} & 0 \\ 0 & 0 & 0 \end{pmatrix}$$

$$\mathbf{C}_\xi = \begin{pmatrix} 0 & 0 & 0 \\ 0 & 0 & -1 \\ 0 & -1 & 0 \end{pmatrix}$$

$$\mathbf{C}_\eta = \begin{pmatrix} 0 & 0 & -1 \\ 0 & 0 & 0 \\ -1 & 0 & 0 \end{pmatrix}$$

$$\mathbf{C}_\zeta = \begin{pmatrix} 0 & -1 & 0 \\ -1 & 0 & 0 \\ 0 & 0 & 0 \end{pmatrix} \qquad (2)$$

The six parts of eq 1 correspond to the six representations (A_{1g}, E_g, and T_{2g}) and their components, included in the symmetrized direct products $T_{1g}\otimes T_{1g} = T_{2g}\otimes T_{2g}$, K_ϵ and K_τ are the harmonic force constants for the ϵ_g and τ_{2g} vibrational modes, V_ϵ and V_τ are the linear JT coupling constants for the $T_g\otimes\epsilon_g$ and $T_g\otimes\tau_{2g}$ problems, W is a quadratic constant, which arises from the coupling between the ϵ_g and τ_{2g} vibrations, and L_ϵ, L_τ, and X_τ refer to quadratic coupling constants, which result from the non-totally-symmetric parts of the $\epsilon_g\times\epsilon_g$ and $\tau_{2g}\times\tau_{2g}$ symmetrized direct products ($e_g(L_\epsilon)$ and $e_g(L_\tau)$ + $t_{2g}(X_\tau)$, respectively).

It has been shown in a symmetry analysis[12] that distortions along the ϵ_g and τ_{2g} modes lead to a decrease of the symmetry toward subgroups of O_h, in which one or more components of these modes become totally symmetric. Activation of ϵ_g lowers the symmetry toward D_{4h} and D_{2h}, where only one (Q_θ) and two (Q_θ and Q_ϵ) components, respectively, are totally symmetric (see Table 1). Activation of τ_{2g} leads to D_{3d}, C_{2h}, and C_i symmetries, where one, two, and three components of the τ_{2g} vibration are totally symmetric. From Table 1 it follows that activation of both ϵ_g and τ_{2g} leads to symmetries which cannot be higher than D_{2h}. The highest possible symmetry which can be achieved upon distortion along a certain vibrational mode or a combination of various modes is referred to as the epikernel symmetry. D_{4h} and D_{3d} are higher and D_{2h} and C_{2h} are lower ranking epikernels. The

TABLE 1: Symmetry Species Spanned by t_{2g} Orbitals and the t_{2g} and e_g Vibrations[a] Involved in the $T_g\otimes(\epsilon_g+\tau_{2g})$ ($T_g = {}^2T_{2g}$ (t_{2g}^1, t_{2g}^5), ${}^3T_{1g}$ (t_{2g}^2, t_{2g}^4)) JT Effect of Transition-Metal Complexes

O_h	D_{4h}^{z}	D_{3d}^{xyz}	D_{2h}^{xy}	C_{2h}^{xy}	C_i
t_{2g}	b_{2g}	a_{1g}	a_g	a_g	a_g
	e_g	e_g	b_{2g}	a_g	a_g
			b_{3g}	b_g	a_g
e_g	a_{1g}	e_g	a_g	a_g	a_g
	b_{1g}		b_{1g}	b_g	a_g

[a] For species spanned by the e_g and t_{2g} vibrations (ϵ_g, τ_{2g}, etc.), Greek letters have been used in the text.

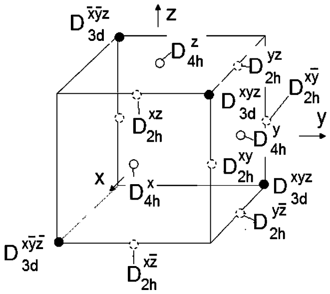

Figure 2. Stationary points of D_{4h}, D_{3d}, and D_{2h} symmetry on the ground-state potential energy surface, which originate from $T_g\otimes(\epsilon_g+\tau_{2g})$ JT coupling.

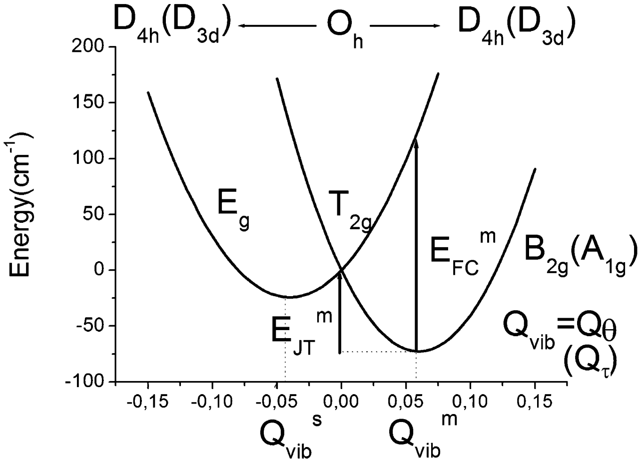

Figure 3. Energy profile for the components split from the $T_g = T_{2g}$ ground states for $d^{1,5}$ (and similarly for $d^{2,4}$) transition-metal ions due to $T_g\otimes\epsilon_g$ ($T_g\otimes\tau_{2g}$) JT coupling along a distortion pathway which preserves the highest possible symmetry D_{4h} (D_{3d}) and lifts the orbital degeneracy. The basic model parameters—the JT stabilization energy, E_{JT}^{m}, the energy of the vertical (Franck−Condon) transition at the D_{4h} (D_{3d}) minimum, E_{FC}^{m}, and the distortions of the active mode, Q_{vib}^{m} and Q_{vib}^{s} (vib = ϵ_g, τ_{2g})—for the minima (m) and saddle points (s) are illustrated.

lowest possible symmetry that can be achieved by the $T_g\otimes(\epsilon_g+\tau_{2g})$ vibronic interaction is C_i and is referred to as a kernel symmetry. It was demonstrated in a case study of the tetrahedral $T\otimes(\epsilon+\tau_2)$ JT effect that extrema prefer epikernels to kernels and maximal epikernels to lower ranking epikernels (epikernel principle).[12]

b. Linear $T_g\otimes(\epsilon_g+\tau_{2g})$ Vibronic Coupling: Determination of the Vibronic Parameters from DFT. The matrix **H** of eq 1 takes the form of eq 3. Coordinates of the stationary points

$$\mathbf{H_1} = \begin{bmatrix} V_\epsilon\cdot\left(\frac{1}{2}Q_\theta - \frac{\sqrt{3}}{2}Q_\epsilon\right) & -V_\tau Q_\zeta & -V_\tau Q_\eta \\ -V_\tau Q_\zeta & V_\epsilon\cdot\left(\frac{1}{2}Q_\theta + \frac{\sqrt{3}}{2}Q_\epsilon\right) & -V_\tau Q_\xi \\ -V_\tau Q_\eta & -V_\tau Q_\xi & -V_\epsilon Q_\theta \end{bmatrix} + \left[\frac{1}{2}K_\epsilon(Q_\theta^{\,2}+Q_\epsilon^{\,2}) + \frac{1}{2}K_\tau(Q_\xi^{\,2}+Q_\eta^{\,2}+Q_\zeta^{\,2})\right]\mathbf{I} \quad (3)$$

on the ground-state potential energy surface can be derived by the method of Öpik and Price (see the Supporting Information).[29] There are three, four, and six symmetry-equivalent points of D_{4h}, D_{3d}, and D_{2h} symmetry. These can be visualized as the axes, corners, and edges of a cube (Figure 2). An energy diagram plot with a single configurational coordinate (Figure 3) illustrates the basic geometric and energetic parameters of the model. These are the tetragonal (D_{4h}) or trigonal (D_{3d}) elongations or compressions of an octahedron (tetragonal: $Q_\theta > 0$ (elongation), $Q_\theta < 0$ (compression); trigonal: $Q_\tau = Q_\xi = Q_\eta = Q_\zeta$; $Q_\tau < 0$ (elongation), $Q_\tau > 0$ (compression)), the Jahn−Teller stabilization energy (E_{JT}^{m}) and the energy of the vertical electronic transition from the minimum of the nondegenerate ground state to the doubly degenerate excited state (E_{FC}^{m}; Franck−Condon, FC). Table 2 gives for the three types of stationary points the corresponding energy functions, derived from the vibronic coupling constants. It is remarkable that in the linear coupling case only four parameters are needed to determine the ground-state topology: i.e., V_ϵ, K_ϵ (for D_{4h} distortions) and V_τ, K_τ (for D_{3d} distortions) (see Table 2). With the following approach one can get these parameters from DFT.

1. A geometry optimization in D_{4h} is performed by using the orbital occupations appropriate for the nondegenerate ground state of interest ($^2B_{2g}$ (d^1, low-spin d^5), $^3A_{2g}$ (d^2, low-spin d^4)); more explicitly, these are the configurations b_{2g}^{1} (Ti^{III}), e_g^{2}(V^{III}), $b_{2g}^{2}e_g^{2}$ (Mn^{III}, Cr^{II}), and $e_g^{4}b_{2g}^{1}$ (Fe^{III}, Mn^{II}). As a result, the metal−ligand bond distances for the axial and equatorial bonds (R_{ax}^{tt}, R_{eq}^{tt}; Figure 4) are obtained and used to calculate Q_θ^{m} with the expressions from Table 4a.

2. With the geometry of step 1 one calculates $E_{FC}^{m}(D_{4h})$ as the difference between the energy of the excited (^2E_g or ^3E_g) and ground states ($^2B_{2g}$ or $^3A_{2g}$) for $d^{1,5}$ and $d^{2,4}$.

3. A geometry optimization in D_{3d} is then performed to yield the orbital occupations of the nondegenerate ground states of interest ($^2A_{1g}$ (d^1, low-spin d^5), $^3A_{2g}$ (d^2, low-spin d^4)); more explicitly, these are the configurations a_{1g}^{1} (Ti^{III}), e_g^{2} (V^{III}), $a_{1g}^{2}e_g^{2}$ (Mn^{III}, Cr^{II}), and $e_g^{4}a_{1g}^{1}$ (Fe^{III}, Mn^{II}). The distance R_{tr} and the angle θ (Figure 4) quantify the trigonal distortion and are used to calculate Q_τ^{m} with the expressions from Table 4b.

4. With the geometry of step 3 one calculates $E_{FC}^{m}(D_{3d})$ as the difference between the energy of the excited (^2E_g or ^3E_g) and ground states ($^2A_{1g}$ or $^3A_{2g}$) for $d^{1,5}$ or $d^{2,4}$.

From the equations in Table 2, V_ϵ, K_ϵ, V_τ, and K_τ are

$$V_\epsilon = \frac{2}{3}\frac{E_{FC}{}^{m}(D_{4h})}{Q_\theta{}^{m}} \quad K_\epsilon = \frac{2}{3}\frac{E_{FC}{}^{m}(D_{4h})}{(Q_\theta{}^{m})^2} \qquad (4)$$

$$V_\tau = \frac{1}{3}\frac{E_{FC}{}^{m}(D_{3d})}{Q_\tau{}^{m}} \quad K_\tau = \frac{2}{9}\frac{E_{FC}{}^{m}(D_{3d})}{(Q_\theta{}^{m})^2} \qquad (5)$$

After substitution in the equations of Table 2 the JT stabilization energies ($E_{JT}^{m}(D_{4h})$ and $E_{JT}^{m}(D_{3d})$] and all quantities, which characterize the D_{2h} stationary points are obtained.

Note that the stabilization of the distorted geometry with respect to the regular octahedral reference (E_{JT}^{m}) does not directly emerge as a difference between the DFT energies of the two configurations but is based on explicit solutions of $\mathbf{H_1}$. This is because Kohn−Sham DFT in its present implementations is not able to calculate the energies of electronic states in the case of orbital degeneracy ($^2T_{2g}$ or $^3T_{1g}$).[30,31] For example, for Ti^{III} (d^1) one electron is distributed evenly between the d_{xz}, d_{yz}, and d_{xy} orbitals. Such a distribution usually leads to a lower energy than the correct one-electron/one-orbital occupancy (no correction for electron self-interaction). Similarily, electronic transitions from a nondegenerate to a doubly degenerate orbital create orbitally degenerate subshells (e_g^{1} in the given example; steps 2 and 4 of the procedure). For a thorough calculation one would adopt the D_{4h} (step 2) or the D_{3d} (step 4) geometry but a D_{2h} or C_s electron distribution, where e_g splits into b_{2g} and b_{3g} or a′ and a″, respectively. Thus, one imposes a single orbital

TABLE 2: Expressions for the Coordinates of the D_{4h}, D_{3d}, and D_{2h} Stationary Points,[a] the JT Stabilization Energies, and Energies of Vertical (Franck−Condon) Transitions[b] for the Linear $T_g\otimes(\epsilon_g+\tau_{2g})$ JT Coupling Problem

D_{4h}	D_{3d}	D_{2h}
$Q_\theta^m(D_{4h}) = V_\epsilon/K_\epsilon$	$Q_\xi^m = Q_\eta^m = Q_\varsigma^m = (2/3)(V_\tau/K_\tau)$	$Q_\theta^{m'}(D_{2h}) = -(1/2)(V_\epsilon/K_\epsilon)$
$Q_\theta^m(D_{4h}) = -V_\epsilon/2K_\epsilon$	$Q_\xi^s = Q_\eta^s = Q_\varsigma^s = -(1/3)(V_\tau/K_\tau)$	$Q_\varsigma^m(D_{2h}) = V_\tau/K_\tau$
$\rho_\epsilon^m(D_{4h}) = \lvert Q_\theta^m(D_{4h})\rvert$	$\rho_\tau^m(D_{3d}) = (2/\sqrt{3})\lvert V_t/K_t\rvert$	$\rho_\epsilon^m(D_{2h}) = (1/2)[\rho_\epsilon^m(D_{4h})]$
		$\rho_\tau^m(D_{2h}) = (\sqrt{3}/2)[\rho_\tau^m(D_{3d})]$
$b_{2g} \rightarrow e_g$	$A_{1g} \rightarrow e_g$	
$E_{FC}^m(D_{4h}) = (3/2)(V_\epsilon^2/K_\epsilon)$	$E_{FC}^m(D_{3d}) = 2(V_\tau^2/K_\tau)$	$E_{FC}^m(D_{2h}, b_{2g}\rightarrow b_{3g}) = E_{FC}^m(D_{3d})$
		$E_{FC}^m(D_{2h}, b_{2g}\rightarrow a_g) = (1/2)[E_{FC}^m(D_{4h}) + E_{FC}^m(D_{3d})]$
$E_{JT}^m(D_{4h}) = (1/2)(V_\epsilon^2/K_\epsilon)$	$E_{JT}^m(D_{3d}) = (2/3)(V_\tau^2/K_t)$	$E_{JT}^m(D_{2h}) = (1/4)[E_{JT}^m(D_{4h})] + (3/4)[E_{JT}^m(D_{3d})]$

[a] Only nonzero values for Q_θ, Q_ϵ, Q_ξ, Q_η, and Q_ζ are listed. [b] Specified as electronic transitions between the components split from the t_{2g} orbital of the t_{2g}^1, t_{2g}^5 ($^2T_{2g}$ states) or the t_{2g}^2, t_{2g}^4 ($^3T_{1g}$ states) electronic configurations.

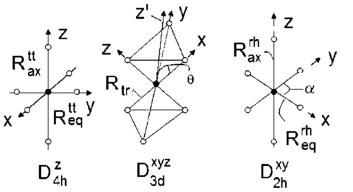

Figure 4. Geometric parameters to describe the JT distortions of $T_g\otimes\epsilon_g$ (D_{4h}^z), $T_g\otimes\tau_{2g}$ (D_{3d}^{xyz}), and $T_g\otimes(\epsilon_g+\tau_{2g})$ (D_{2h}^{xy}) type, deduced from DFT geometry optimizations with electronic configurations with correct spin and space symmetries in D_{4h} ($^2B_{2g}$(d^1, low-spin d^5), $^3A_{2g}$(d^2, low-spin d^4)), D_{3d} ($^2A_{1g}$(d^1, low-spin d^5), $^3A_{2g}$(d^2, low-spin d^4)), and D_{2h} ($^2B_{2g}$(d^1,d^5), $^3B_{2g}$(d^2,d^4)).

occupancy by artificially lowering the symmetry. A full list of orbital occupations derived from this procedure is given in the Supporting Information.

So far, we have considered the symmetry of the nuclear configurations and of the electronic states as well as the distortions of the nuclear coordinates of the stationary points on the ground-state potential energy surface. In order to decide if a stationary point corresponds to a minimum or to a saddle point, the Hamiltonian of eq 3 has to be reexpanded around the extrema in D_{4h}, D_{3d}, and D_{2h} to yield a new Hessian matrix. This differs from that of the octahedron, which is diagonal with the elements K_ϵ and K_τ for the ϵ_g and τ_{2g} vibrations. Diagonalization of the new matrix yields the force constants as the eigenvalues and the principal axes of curvature as the eigenvectors of the Hessian. A minimum implies that all five eigenvectors are positive, while saddle points (transition states for reactions) have one negative eigenvalue (the corresponding eigenvector indicates the reaction coordinate (transition vector)). In D_{4h} symmetry, the τ_{2g} vibration splits into α_{1g} and ϵ_g, and the only mode which can couple the $^2B_{2g}$ (d^1, low-spin d^5) or $^3A_{2g}$ (d^2, low-spin d^4) ground states with the ^2E_g or ^3E_g excited states and yield negative curvature is the ϵ_g (τ_{2g}) mode. Its force constant, $K_{\epsilon_g(\tau_{2g})}$ is given by eq 6 (see the Supporting Information).

$$K_{\epsilon_g(\tau_{2g})} = K_\tau\left(1 - \frac{4}{3}\frac{V_\tau^2 K_\epsilon}{V_\epsilon^2 K_\tau}\right) \tag{6}$$

Therefore, the values V_ϵ, K_ϵ, V_τ, and K_τ, obtained from DFT, are of immediate use to judge whether a given stationary point represents a minimum or a saddle point. For extrema with D_{3d} symmetry there are two vibrations of ϵ_g symmetry, which can mix the $^2A_{1g}$ (d^1, low-spin d^5) or the $^3A_{2g}$ ground state (d^2, low-spin d^4) with the ^2E_g or ^3E_g excited state. One of them arises from the ϵ_g octahedral mode ($\epsilon_g(\epsilon_g)$, which does not split in D_{3d} symmetry), the other ($\epsilon_g(\tau_{2g})$) originates from the τ_{2g} vibrations (vide supra). Therefore, the Hessian is given by a 2 × 2 matrix and a possible instability will be reflected by the negative sign of its lowest eigenvalue.

$$\begin{array}{c} \begin{array}{cc} \epsilon_g(\epsilon_g) & \epsilon_g(\tau_{2g}) \end{array} \\ \begin{bmatrix} K_\epsilon - \frac{1}{2}K_\tau\frac{V_\epsilon^2}{V_\tau^2} & \frac{K_\tau V_\epsilon}{\sqrt{6}V_\tau} \\ \frac{K_\tau V_\epsilon}{\sqrt{6}V_\tau} & \frac{2}{3}K_\tau \end{bmatrix} \end{array} \tag{7}$$

Finally, we note that D_{2h} stationary points originate from the combined action of the $\epsilon_g(Q_\theta)$ and the $\tau_{2g}(Q_\zeta)$ vibrations. The distortion along Q_θ is of opposite sign with respect to that which leads to a nondegenerate ground state. Therefore, it stabilizes an E_g ground state. The role of the $\tau_{2g}(Q_\zeta)$ mode is to split the E_g state into B_{2g} or B_{3g}, depending on the sign of Q_ζ. We focus here on the B_{2g} ground state; the others, derived from the T_g term, are B_{3g} and A_g. The B_{2g} state can mix with A_g via the β_{2g} split component of the $\tau_{2g}(O_h)$ mode, or with the β_{1g} vibration of the $\epsilon_g(O_h)$ mode. The following equations for their force constants emerge (see Supporting Information):

$$K_{\beta_{2g}} = K_\tau\left(1 - \frac{8K_\epsilon}{4K_\epsilon + 3K_\tau\dfrac{V_\epsilon^2}{V_\tau^2}}\right) \tag{8}$$

$$K_{\beta_{1g}} = K_\epsilon\left(1 - \frac{3}{4}\frac{V_\epsilon^2}{V_\tau^2}\cdot\frac{K_\tau}{K_\epsilon}\right) \tag{9}$$

Stationary points with D_{2h} symmetry may represent genuine transition states in contrast to the extrema in D_{4h} and D_{3d} symmetry, where only ϵ_g vibrations can contribute to instability and lead to second-order or higher order saddle points. This is of importance for the reactivity of the systems.

c. Quadratic $T_g\otimes(\epsilon_g+\tau_{2g})$Vibronic Coupling: Determination of All Parameters of the Vibronic Hamiltonian from DFT. The extension of the DFT approach to the more general case of quadratic $T_g\otimes(\epsilon_g+\tau_{2g})$ JT coupling is straightforward. As in the linear case, we subdivide the procedure to get the vibronic coupling parameters into the $T_g\otimes\epsilon_g$ (D_{4h}) and $T_g\otimes\tau_{2g}$ (D_{3d}) sections (steps 1 and 2), in which the ϵ_g and τ_{2g} vibrations are decoupled from each other, and into a combined $T_g\otimes(\epsilon_g+\tau_{2g})$ (D_{2h}) problem (step 3), which allows us to get all $T_g\otimes\epsilon_g-T_g\otimes\tau_{2g}$ coupling terms. In step 1, we have the following expressions for the distortion along Q_θ for the nondegenerate ($^2B_{2g}$($^2T_{2g}$) or $^3A_{2g}$($^3T_{1g}$)) (Q_θ^m) and the doubly degenerate (^2E_g($^2T_{2g}$) or ^3E_g($^3T_{1g}$)) (Q_θ^s) electronic states[12]

$$Q_\theta{}^{\mathrm{m}} = \frac{V_\epsilon}{K_\epsilon + L_\epsilon}$$

$$Q_\theta{}^{\mathrm{s}} = -\frac{V_\epsilon}{2K_\epsilon - L_\epsilon} \tag{10}$$

and in addition, for the energy of the FC transition at $Q_\theta{}^{\mathrm{m}}$ ($E_{\mathrm{FC}}{}^{\mathrm{m}}(D_{4h})$)

$$E_{\mathrm{FC}}{}^{\mathrm{m}}(D_{4h}) = \frac{3}{2}\left(K_\epsilon + \frac{1}{2}L_\epsilon\right)(Q_\theta{}^{\mathrm{m}})^2 \tag{11}$$

Here, the parameters V_ϵ, L_ϵ, and K_ϵ are obtained from the values of $Q_\theta{}^{\mathrm{m}}$, $Q_\theta{}^{\mathrm{s}}$, and $E_{\mathrm{FC}}{}^{\mathrm{m}}(D_{4h})$, deduced from DFT. In step 2, we have the following expressions for the distortion along Q_τ ($=Q_\xi = Q_\eta = Q_\zeta$) for the nondegenerate (${}^2\mathrm{A}_{1g}({}^2\mathrm{T}_{2g})$ or ${}^3\mathrm{A}_{2g}({}^3\mathrm{T}_{1g})$) ($Q_\tau{}^{\mathrm{m}}$) and the doubly degenerate (${}^2\mathrm{E}_{g}({}^2\mathrm{T}_{2g})$ or ${}^3\mathrm{E}_{g}({}^3\mathrm{T}_{1g})$) ($Q_\theta{}^{\mathrm{s}}$) electronic states[12]

$$Q_\tau{}^{\mathrm{m}} = \frac{2V_\tau}{3K_\tau - 4X_\tau}$$

$$Q_\tau{}^{\mathrm{s}} = -\frac{V_\tau}{3K_\tau + 2X_\tau} \tag{12}$$

and in addition for the energy of the FC transition at $Q_\theta{}^{\mathrm{m}}$ ($E_{\mathrm{FC}}{}^{\mathrm{m}}(D_{3d})$)

$$E_{\mathrm{FC}}{}^{\mathrm{m}}(D_{3d}) = \frac{3}{2}(3K_\tau - 2X_\tau)(Q_\tau{}^{\mathrm{m}})^2 \tag{13}$$

The parameters V_τ, X_τ, and K_τ are obtained from the values of $Q_\theta{}^{\mathrm{m}}$, $Q_\theta{}^{\mathrm{s}}$, and $E_{\mathrm{FC}}{}^{\mathrm{m}}(D_{3d})$, deduced from DFT. Finally, in step 3, we consider a DFT geometry optimization for a ${}^2\mathrm{B}_{2g}({}^2\mathrm{T}_{2g})$ or a ${}^3\mathrm{B}_{2g}({}^3\mathrm{T}_{1g})$ ground state, which leads to a D_{2h} distorted geometry. At this stationary point the distortions along Q_θ and Q_ζ ($Q_\theta{}^{\mathrm{m}'}$ and $Q_\varsigma{}^{\mathrm{m}}$, respectively) are given by[12]

$$Q_\theta{}^{\mathrm{m}'} = \frac{-V_\epsilon + 2WQ_\varsigma{}^{\mathrm{m}}}{2K_\epsilon - L_\epsilon}$$

$$Q_\varsigma{}^{\mathrm{m}} = \frac{2V_\tau + 2WQ_\theta{}^{\mathrm{m}'}}{2K_\tau - L_\tau} \tag{14}$$

The distortions are calculated from structural data from DFT geometry optimizations, with bond distances to get $Q_\theta{}^{\mathrm{m}'}$ and angles to get $Q_\varsigma{}^{\mathrm{m}}$. With the parameters V_ϵ, V_τ, K_ϵ, L_ϵ, and K_τ, available from steps 1 and 2, the parameters W and L_τ are obtained. Therefore, we have expressed the parameters of the Hamiltonian **H** (eq 1) in terms of data which are all based on DFT (see Appendix for the master equations). From these parameters JT stabilization energies for the D_{4h}, D_{3d}, and D_{2h} stationary points may be obtained:[12]

$$E_{\mathrm{JT}}{}^{\mathrm{m}}(D_{4h}) = \frac{1}{2}\frac{V_\epsilon{}^2}{K_\epsilon + L_\epsilon} = \frac{1}{2}V_\epsilon Q_\theta{}^{\mathrm{m}} \tag{15}$$

$$E_{\mathrm{JT}}{}^{\mathrm{m}}(D_{3\mathrm{d}}) = \frac{2V_\tau{}^2}{3K_\tau - 4X_\tau} = V_\tau Q_\tau{}^{\mathrm{m}} \tag{16}$$

$$E_{\mathrm{JT}}{}^{\mathrm{m}}(D_{2h}) = \frac{V_\epsilon{}^2K_\tau' + 4V_\tau{}^2K_\epsilon' - 4WV_\epsilon V_\tau}{8(K_\epsilon'K_\tau' - W^2)} \tag{17}$$

$$K_\epsilon' = K_\epsilon - \frac{1}{2}L_\epsilon \quad K_\tau' = K_\tau - \frac{1}{2}L_\tau$$

An analysis of the topology of the ground-state potential energy surface in the vicinity of each stationary point of $D_{4\mathrm{h}}$, D_{3d}, and D_{2h} symmetry is possible, as described in detail in section IIb. Analytical expressions of the noninteracting modes and their diagonal Hessian matrix elements are given in Table 3. Vibronic mixing (distortions away from the D_{4h}, D_{3d}, and D_{2h} stationary point geometries) between electronic states induces off-diagonal matrix elements, which can cause instabilities of the kind already described in section IIb. However, analytical expressions, similar to those of eqs 6−9, are quite cumbersome in this case. For this reason, we resort to numerical calculations of the (5 × 5) Hessian matrix (see the Supporting Information).

d. Static Strain and the Dynamic Jahn−Teller Effect. Calculations of the temperature dependence of the magnetic susceptibility and the **g** tensors have been done for $[\mathrm{Fe(CN)_6}]^{3-}$ (section Vb). The Hamiltonian of the problem is written as a sum (eq 18) where the first to fourth terms are the ligand field, interelectronic repulsion, spin−orbit coupling, and Zeeman energy operators. These have been parametrized with the cubic ligand field splitting ($10Dq$, $\hat{\mathrm{H}}_{\mathrm{LF}}$), the interelectronic repulsion (B and C, $\hat{\mathrm{H}}_{\mathrm{IER}}$), the spin−orbit coupling (ζ, $\hat{\mathrm{H}}_{\mathrm{SO}}$), and the covalent reduction parameters (k, $\hat{\mathrm{H}}_{\mathrm{Z}} = \mu_{\mathrm{B}}\mathbf{B}(\mathbf{S} + k\mathbf{L})$), respectively. As will be shown in section IVa, vibronic coupling to the τ_{2g} mode dominates and $\hat{H}_{\mathrm{vib}}$ is

$$\hat{H} = \hat{H}_{\mathrm{LF}} + \hat{H}_{\mathrm{IER}} + \hat{H}_{\mathrm{SO}} + \hat{H}_{\mathrm{Z}} + \hat{H}_{\mathrm{vib}} + \hat{H}_{\mathrm{JT}} + \hat{H}_{\mathrm{str}} \tag{18}$$

$$\hat{H}_{\mathrm{vib}} = \frac{1}{2}\hbar\omega_\tau(\hat{P}_\xi{}^2 + \hat{P}_\eta{}^2 + \hat{P}_\zeta{}^2 + Q_\xi'^2 + Q_\eta'^2 + Q_\zeta'^2) \tag{19}$$

where $\hbar\omega_\tau$ is the energy of the three-dimensional harmonic oscillator and $\hat{P}_{\mathrm{i}}$ and Q_{i}' are dimensionless operators, related to the observables for momentum and position.[32]

$$\hat{P}_{\mathrm{i}} = \frac{1}{\sqrt{\mu\hbar\omega}}\hat{p}_{\mathrm{i}}$$

$$Q_{\mathrm{i}}' = \sqrt{\frac{\mu\omega}{\hbar}}Q_{\mathrm{i}}$$

$$\mathrm{i} = \xi, \eta, \zeta \tag{20}$$

Up to the vibronic eigenvalue problem, we restrict the treatment to linear $\mathrm{T}_{2g}\otimes\tau_{2g}$ terms in $\hat{H}_{\mathrm{JT}}$ ($Q_\theta = Q_\epsilon = 0$ in eq 3).

We use the distortions given by the geometric lattice strain ($Q_\xi{}^{\mathrm{s}}$, $Q_\eta{}^{\mathrm{s}}$, and $Q_\zeta{}^{\mathrm{s}}$, deduced from structural data) and the vibronic coupling constants (up to second order) for $[\mathrm{Fe(CN)_6}]^{3-}$ to approximate the strain matrix $\mathbf{H_{str}}$:

$$\mathbf{H_{str}} =$$

$$\begin{array}{c} \xi(yz) \\ \eta(xz) \\ \zeta(xy) \end{array} \begin{bmatrix} \frac{1}{4}L_\tau(2(Q_\xi{}^s)^2 - (Q_\eta{}^s)^2 - (Q_\varsigma{}^s)^2) & -V_\tau Q_\varsigma{}^s - X_\tau Q_\xi{}^s Q_\eta{}^s & -V_\tau Q_\eta{}^s - X_\tau Q_\xi{}^s Q_\varsigma{}^s \\ -V_\tau Q_\varsigma{}^s - X_\tau Q_\xi{}^s Q_\eta{}^s & \frac{1}{4}L_\tau(2(Q_\eta{}^s)^2 - (Q_\varsigma{}^s)^2 - (Q_\xi{}^s)^2) & -V_\tau Q_\xi{}^s - X_\tau Q_\eta{}^s Q_\varsigma{}^s \\ -V_\tau Q_\eta{}^s - X_\tau Q_\xi{}^s Q_\varsigma{}^s & -V_\tau Q_\xi{}^s - X_\tau Q_\eta{}^s Q_\varsigma{}^s & \frac{1}{4}L_\tau(2(Q_\varsigma{}^s)^2 - (Q_\xi{}^s)^2 - (Q_\eta{}^s)^2) \end{bmatrix} \quad (21)$$

The following procedure was adopted to set up the vibronic Hamiltonian. All matrices, which represent $\hat{H}$ (eq 18, excluding $\hat{H}_{vib}$), are calculated with the basis of all 256 Slater determinants of the d^5 configuration of $[Fe(CN)_6]^{3-}$. The matrix $\mathbf{H_{LF}} + \mathbf{H_{IER}} + \mathbf{H_{SO}} + \mathbf{H_{str}}$ was diagonalized first. The lowest six eigenvectors and eigenvalues, related to the parent octahedral $^2T_{2g}$ term, take the configuration interaction (CI) into account. This is important for all complexes (except for $[Ti(CN)_6]^{3-}$; see section IVb). The (256 × 6) matrix of the lowest six eigenvectors $\mathbf{C}$ is used to reduce the size of $\mathbf{H_{JT}}$ and $\mathbf{H_Z}$ (256 × 256) to 6 × 6 matrices $\mathbf{H_{JT}}^{\mathbf{r}}$ and $\mathbf{H_Z}^{\mathbf{r}}$, written within the subspace of the three lowest Kramers doublets:

$$\mathbf{H_{JT}}^{\mathbf{r}} = \boldsymbol{C}^{+}\boldsymbol{H}_{\mathbf{JT}}\boldsymbol{C} \quad (22)$$

$$\mathbf{H_{Z}}^{\mathbf{r}} = \boldsymbol{C}^{+}\boldsymbol{H}_{\mathbf{Z}}\boldsymbol{C} \quad (23)$$

Calculations of the $\mathbf{g}$ and susceptibility tensors in this step yield the results in section Vb.1. For the dynamic JT effect we express the vibronic eigenfunctions of the total Hamiltonian $\mathbf{H}$, Ψ as a linear combination of products of the lowest six exact electronic eigenfunctions of $\mathbf{H_{LF}} + \mathbf{H_{IER}} + \mathbf{H_{SO}} + \mathbf{H_{str}}$, φ_i, and the states of the three-dimensional harmonic oscillator $[\chi_j(Q_\xi')][\chi_k(Q_\eta')][\chi_\zeta(Q_\xi')]$ up to the level n_v:

$$\Psi = \sum_{i=1}^{6}\sum_j\sum_k\sum_l\sum_{j+k+l=0}^{n_v} c_{ijkl}\varphi_i\chi_j(Q_\xi')\chi_k(Q_\eta')\chi_l(Q_\zeta') \quad (24)$$

The total basis size N_v without exploitation of the vibronic symmetries is given by:

$$N_v = 6\left[\frac{n_v(n_v{}^2 + 6n_v + 11)}{6} + 1\right] \quad (25)$$

For the moderate vibronic coupling strength, obtained for $[Fe(CN)_6]^{3-}$ (section IVa), accurate $\mathbf{g}$ tensor values and magnetic susceptibilities (≤2%) are achieved with $n_v = 10$, leading to a total dimension of the vibronic matrix of 1716 × 1716.

e. Effect of Pseudo Jahn−Teller Coupling. Vibronic parameters are deduced from DFT geometry optimizations. Therefore, they include possible contributions from pseudo JT mixing. Without loss of generality, we take $[Ti(CN)_6]^{3-}$ as an example and consider the vibronic mixing (via the τ_{2g} distortions) of its $^2T_{2g}(\xi,\eta,\zeta)$ electronic ground state with the $^2E_g(\theta,\epsilon)$ excited state, quantified by the matrix elements[33]

$$\begin{bmatrix} & |T_{2g}(\xi)\rangle & |T_{2g}(\eta)\rangle & |T_{2g}(\zeta)\rangle \\ \langle E_g(\theta)| & -\frac{1}{2}P_\tau Q_\xi & -\frac{1}{2}P_\tau Q_\eta & P_\tau Q_\eta \\ \langle E_g(\epsilon)| & \frac{\sqrt{3}}{2}P_\tau Q_\xi & -\frac{\sqrt{3}}{2}P_\tau Q_\xi & 0 \end{bmatrix} \quad (26)$$

P_τ is the pseudo JT vibronic coupling parameter, defined as

$$P_\tau = \left\langle \zeta \left| \left(\frac{\partial V}{\partial Q_\varsigma}\right)_0 \right| \theta \right\rangle \quad (27)$$

CN^- is a strong-field ligand (Table 7), i.e. the energy difference $^2E_g - {}^2T_{2g}$ ($\Delta = 10Dq$) is large, and it is possible to apply perturbation theory to obtain the following matrix to describe the pseudo JT effect within the $^2T_{2g}(\xi,\eta,\zeta)$ electronic state:

TABLE 3: Normal-Mode Analysis of the D_{4h}, D_{3d}, and D_{2h} Stationary Points of the $T_g\otimes(\epsilon_g+\tau_{2g})$ J T Surface

extremal points	ground state	excited states	normal modes and expressions for the associated force constants at the position of the D_{4h}, D_{3d}, and D_{2h} extremal points[a]	distortions causing eventual instabilities[b]
D_{4h}	B_{2g} (A_{2g})	E_g	α_{1g}, Q_θ; $K_\epsilon + L_\epsilon$	none
			β_{1g}, Q_ϵ; $K_\epsilon - L_\epsilon$	none
			β_{2g}, Q_ζ; $K_\tau + L_\tau$	none
			ϵ_g, (Q_ξ, Q_η); $K_\tau - L_\tau/2$	$\epsilon_g\,(\tau_{2g})$
D_{3d}	A_{1g} (A_{2g})	E_g	ϵ_g, (Q_θ, Q_ϵ); K_ϵ	$\epsilon_g\,(\epsilon_g)$
			α_{1g}, $(1/\sqrt{3})(Q_\xi + Q_\eta + Q_\zeta)$; $K_\tau - (4/3)X_\tau$	none
			ϵ_g, $(1/\sqrt{6})(2Q_\zeta - Q_\xi - Q_\eta)$; $K_\tau + (2/3)X_\tau$	$\epsilon_g\,(\tau_{2g})$
			$(1/\sqrt{2})(Q_\xi - Q_\eta)$; $K_\tau + (2/3)X_\tau$	
D_{2h}	B_{2g}	B_{3g}, A_{1g}	β_{1g}, Q_ϵ; $K_\epsilon' + L_\epsilon$	β_{1g}
			$\left.\begin{matrix}\alpha_g(Q_\theta)\\ \alpha_g(Q_\varsigma)\end{matrix}\right]\Bigg\} \frac{K_\epsilon' + K_\tau'}{2} \pm \frac{1}{2}\sqrt{(K_\epsilon' - K_\tau')^2 + 4W^2}$	none none
			β_{2g}, $(1/2)(Q_\xi + Q_\eta)$; $K_\tau' + (3/4)L_\tau - X_\tau$	β_{2g}
			β_{3g}, $(1/2)(Q_\xi - Q_\eta)$; $K_\tau' + (3/4)L_\tau + X_\tau$	none
	B_{3g}	B_{2g}, A_{1g}	β_{1g}, Q_ϵ; $K_\epsilon' + L_\epsilon$	β_{1g}
			$\left.\begin{matrix}\alpha_g(Q_\theta)\\ \alpha_g(Q_\varsigma)\end{matrix}\right]\Bigg\} \frac{K_\epsilon' + K_\tau'}{2} \pm \frac{1}{2}\sqrt{(K_\epsilon' - K_\tau')^2 + 4W^2}$	none none
			β_{2g}, $(1/2)(Q_\xi + Q_\eta)$; $K_\tau' + (3/4)L_\tau + X_\tau$	none
			β_{3g}, $(1/2)(Q_\xi - Q_\eta)$; $K_\tau' + (3/4)L_\tau - X_\tau$	β_{3g}

[a] $K_\epsilon' = K_\epsilon - L_\epsilon/2$; $K_\tau' = K_\tau - L_\tau/2$. [b] Possible transition states (first-order saddle points) are underlined.

$$\begin{array}{ccc} |T_{2g}(\xi)\rangle & |T_{2g}(\eta)\rangle & |T_{2g}(\zeta)\rangle \\ \left[\begin{array}{ccc} -\dfrac{P_\tau^{\ 2}}{\Delta}Q_\xi^{\ 2} & 0 & 0 \\ 0 & -\dfrac{P_\tau^{\ 2}}{\Delta}Q_\eta^{\ 2} & 0 \\ 0 & 0 & -\dfrac{P_\tau^{\ 2}}{\Delta}Q_\zeta^{\ 2} \end{array}\right] \end{array} \tag{28}$$

It follows that the pseudo JT coupling modifies the diagonal quadratic JT coupling terms of the $T_g \otimes \tau_{2g}$ problem (L_τ term in eq 1). To obtain an estimate for the value of P_τ, we will focus on $[Fe(CN)_6]^{3-}$ and try to exclude the contribution from the $T_{2g} \otimes \tau_{2g}$ JT coupling. We achieve this by addition of an electron to the t_{2g}^5 configuration, leading to a $^1A_{1g}(t_{2g}^6)$ ground state. We restrict the analysis to trigonal (D_{3d}) elongations or compressions (component of the τ_{2g} mode, $\alpha_{1g} = 1/\sqrt{3}(Q_\xi + Q_\eta + Q_\zeta)$; it will be shown in section IVa that these distortions are energetically preferred). The mixing between the $^1A_{1g}(t_{2g}^6)$ ground state with the $^1A_{1g}(t_{2g}^5e_g^1)$ excited state ($^1T_{1g}(t_{2g}^5e_g^1)$) is described by the matrix:

$$\begin{array}{cc} |^1A_{1g}(t_{2g}^{\ 6}\rangle & |^1A_{1g}(t_{2g}^{\ 5}e_g^{\ 1}\rangle \\ \left[\begin{array}{cc} E_g & N_\tau \\ N_\tau & E_e \end{array}\right] \end{array} \tag{29}$$

E_g and E_e are the ground- and excited-state energies (E_g is zero in O_h geometry), and N_τ describes their mixing. A method has been proposed to derive these energies from DFT.[34,35] We focus on the lowest eigenvalue $E\_$ of eq 29 and can represent it as

$$E\_ = E_{rf} - E_{vib} \tag{30}$$

E_{rf} ($=E_g$) and E_{vib} are the restoring elastic and the vibronic stabilization energies (both defined to be positive), which oppose and support the α_{1g} (τ_{2g}) D_{3d} distortion, respectively. A series of DFT calculations have been performed to obtain $E\_$, E_{rf}, and E_{vib} for this model example. They are represented in Figure 5 and suggest the absence of the pseudo JT instability. From these calculations we have also derived the value of N_τ (see Figure 5):

$$N = P_{\alpha_{1g}}Q_{\alpha_{1g}} = 3P_\tau Q_\tau \tag{31}$$

N_τ is found to depend linearly on Q_τ with a resulting value of $P_\tau = 3827$ cm^{-1}/Å. With $\Delta = 34\,950$ cm^{-1} (Table 7) we obtain a value of 419 cm^{-1}/Å for the pseudo JT coupling energy (P_τ^2/Δ). This may be considered as included in an efficient way in the vibronic coupling constant L_τ (1584 cm^{-1}/Å^2; see Table 5). The second-order terms (JT and pseudo JT) do not yield leading contributions to the topology of the ground-state potential energy surface (see section IVa).

III. Computational and Experimental Details

All DFT calculations were carried out with the Amsterdam Density Functional program (ADF).[36] In a case study on $[Mn(CN)_6]^{3-}$ ($T_g \otimes \epsilon_g$ problem)[11] it was shown that vibronic coupling constants do not significantly depend on the functional. Since the LDA-VWN functional[37] is known to perform better than GGA for geometries of transition-metal complexes, in particular for metal−ligand bond distances, we have chosen LDA in all calculations. Large Slater-type orbital basis sets (STO, triple-ζ) with one polarization function (p type for H, d type for C and N) and the frozen-core approximation up to 3p for metal ions and 1s for carbon and nitrogen were used. To account for the negative charges, calculations on charge-compensated species ($[M^{III}(CN)_6]^{3-}{}_{solv}$ and $[M^{II}(CN)_6]^{4-}{}_{solv}$) were done with the conductor-like screening model COSMO,[38] implemented in ADF.[39] The dielectric constant of water ($\epsilon = 78.4$) was used with the solvent radii of 1.00 Å (M = Cr, Mn, Fe), 2.10 Å (C), and 1.40 Å (N).

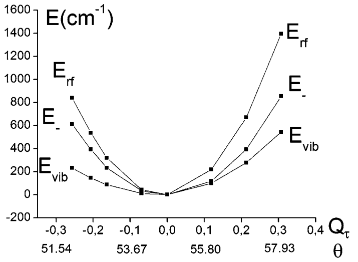

Figure 5. Dependence of E_-, E_{rf}, and E_{vib} on the trigonal distortion parameters Q_τ and θ for $[Fe(CN)_6]^{4-}$. Numerical values of the (Q_τ, N_τ) pairs (in units of Å and cm^{-1}, respectively, not shown, but calculated) are as follows: (−0.257, 2951); (−0.206, 2350); (−0.163, 1817); (−0.069; 609); (0.119, −1953); (0.213, −3247); (0.307, −4526).

Synthesis. $K_3[Mn(CN)_6]$ was prepared as described in the literature.[40] Large single crystals were grown by slow evaporation from an aqueous solution.

Vis−Near-IR Spectroscopy. A single crystal ($d \approx 3$ mm) was placed to cover a small aperture on a copper plate, which was attached to the sample holder of an optical closed cycle cryosystem (Oxford Instruments, CCC1100T), capable of reaching sample temperatures of 11 K with the sample sitting in a helium exchange gas atmosphere for efficient cooling. Absorption spectra were recorded on a Fourier transform spectrometer (Bruker IFS 66), equipped with light sources, beam splitters, and detectors to cover the spectral range from 6000 to 30 000 cm^{-1} at a spectral resolution of better than 2 cm^{-1}.

IV. Results and Discussion

a. Topology of the Ground-State Potential Energy Surface of $M(CN)_6$ Complexes with JT-Active T_g Ground States. A collection of geometric data of JT-distorted structures in D_{4h}, D_{3d}, and D_{2h} symmetry from DFT geometry optimizations is given in Table 4. The parameters which describe these distortions are defined in Figure 4. There are two types of bond lengths for D_{4h} geometries (axial and equatorial, R_{ax}^{tt}, R_{eq}^{tt}), the trigonal angle θ and the bond distance R_{tr} for D_{3d} geometries and the two bond lengths (R_{eq}^{rh} and R_{ax}^{rh}) and the angle α for the D_{2h} geometries. Distortions of the same sign are predicted for D_{4h} and D_{3d}: i.e., tetragonally and trigonally elongated octahedra for Ti^{III}, Mn^{III}, and Cr^{II} and compressed octahedra for V^{III}, Fe^{III}, and Mn^{II}. There is a strict correspondence between the electron count and the sign of the distortion (i.e., elongations for $d^{1,4}$ and compressions for $d^{2,5}$), and the magnitude of the distortion correlates with the π-back-bonding character of the metal−cyanide bond. For a given oxidation state, π-back-donation increases from left to right of the 3d series,[41] and it also increases with the decrease of the oxidation state for a given metal ion. The $|Q_\tau^m|$ vs e_π plot in Figure 6 illustrates this correlation. Geometric distortions for complexes of the same ions with π-donor ligands such as F^- and Cl^- are found to follow the opposite trend: D_{4h} and D_{3d} compressed octahedra are predicted for $[TiF_6]^{3-}$.[42] DFT geometries and energies have been used to obtain vibronic coupling parameters and JT stabilization energies $E_{JT}(D_{4h})$, $E_{JT}(D_{3d})$ and $E_{JT}(D_{2h})$, as de-

TABLE 4: Bond Distances (in Å) and Angles (in deg) from D_{4h}, D_{3d}, and D_{2h} Symmetry-Constrained DFT Geometry Optimizations and Energies (in cm^{-1}) of Vertical (Franck−Condon, FC) Electronic Transitions from the Nondegenerate into the Doubly Degenerate (for D_{4h} and D_{3d}) Split Components of the ${}^2T_{2g}$ or ${}^3T_{1g}$ Octahedral Terms at the Energy Minima (m), Used to Calculate the Vibronic Parameters of the $T_{2g}\otimes(e_g+t_{2g})$ Potential Energy Surface up to First- and Second-Order Vibronic Coupling

(a) D_{4h} Stationary Points

complex	${}^2B_{2g}({}^2T_{2g})$ or ${}^3A_{2g}({}^3T_{1g})$ state		${}^2E_g({}^2T_{2g})$ or ${}^3E_g({}^3T_{1g})$ state					E_{FC}^{m} ${}^2B_{2g}\rightarrow{}^2E_g({}^2T_{2g})$ or ${}^3A_{2g}\rightarrow{}^3E_{g}({}^3T_{1g})$
	R_{eq}^{tt}	R_{ax}^{tt}	R_{eq}^{tt}	R_{ax}^{tt}	$Q_\theta^{m\ a}$	$Q_\theta^{s\ a}$	$\lvert r_\epsilon\rvert^b$	
$[Ti(CN)_6^{3-}]_{solv}$	2.168	2.199	2.184	2.168	0.036	−0.018	2.0	173
$[V(CN)_6^{3-}]_{solv}$	2.096	2.079	2.088	2.097	−0.020	0.010	2.0	48
$[Mn(CN)_6^{3-}]_{solv}$	1.948	1.973	1.961	1.948	0.029	−0.015	1.9	158
$[Fe(CN)_6^{3-}]_{solv}$	1.907	1.897	1.902	1.908	-0.011_5	0.007	1.6	14
$[Cr(CN)_6^{4-}]_{solv}$	1.991	2.032	2.011	1.991	0.047	−0.023	2.0	552
$[Mn(CN)_6^{4-}]_{solv}$	1.940	1.912	1.926	1.940	−0.032	0.016	2.0	190

(b) D_{3d} Stationary Points

complex	${}^2A_{1g}({}^2T_{2g})$ or ${}^3A_{2g}({}^3T_{1g})$		${}^2E_g({}^2T_{2g})$ or ${}^3E_g({}^3T_{1g})$					E_{FC}^{m} ${}^2A_{1g}\rightarrow{}^2E_g({}^2T_{2g})$ or ${}^3A_{2g}\rightarrow{}^3E_{g}({}^3T_{1g})$
	θ	R_{tr}	θ	R_{tr}	$Q_\tau^{m\ c}$	$Q_\tau^{s\ c}$	$\lvert r_\tau\rvert^d$	
$[Ti(CN)_6^{3-}]_{solv}$	54.30	2.178	55.38	2.180	−0.047	0.069	0.7	31
$[V(CN)_6^{3-}]_{solv}$	55.82	2.089	54.52	2.092	0.112	−0.022	5.1	206
$[Mn(CN)_6^{3-}]_{solv}$	53.53	1.956	55.60	1.956	−0.116	0.083	1.4	265
$[Fe(CN)_6^{3-}]_{solv}$	56.10	1.904	54.15	1.905	0.128	−0.055	2.3	427
$[Cr(CN)_6^{4-}]_{solv}$	52.89	2.004	55.81	2.003	−0.182	0.106	1.7	1865
$[Mn(CN)_6^{4-}]_{solv}$	56.47	1.932	53.94	1.932	0.165	−0.076	2.2	969

(c) D_{2h} Stationary Points

complex	${}^2B_{2g}({}^2T_{2g})$ or ${}^3B_{2g}({}^3T_{1g})$ state						
	R_{eq}^{rh}	R_{ax}^{rh}	α	$Q_\theta^{m'\ e}$	$Q_\zeta^{m\ e}$	$r_\epsilon'^{\ f}$	$r_\tau'^{\ f}$
$[Ti(CN)_6^{3-}]_{solv}$	2.182	2.168	88.86	−0.016	−0.087	0.9	1.8
$[V(CN)_6^{3-}]_{solv}$	2.087	2.097	87.98	0.011_5	0.147	1.2	1.3
$[Mn(CN)_6^{3-}]_{solv}$	1.961	1.948	88.00	−0.015	−0.137	1.0	1.2
$[Fe(CN)_6^{3-}]_{solv}$	1.902	1.908	87.00	0.007	0.199	1.0	1.6
$[Cr(CN)_6^{4-}]_{solv}$	2.011	1.992	85.82	−0.022	−0.292	1.0	1.6
$[Mn(CN)_6^{4-}]_{solv}$	1.928	1.942	86.34	0.016	0.247	1.0	1.5

[a] Calculated with the R_{eq}^{tt} and R_{ax}^{tt} values and the following set of equations: $Q_\theta = 2(dR_{ax} - dR_{eq})/\sqrt{3}$; $dR_{ax} = R_{ax} - R_{av}$; $dR_{eq} = R_{eq} - R_{av}$; $R_{av} = (2R_{eq} + R_{ax})/3$. [b] $r_\epsilon = Q_\theta^{m}/Q_\theta^{s}$; $r_\epsilon = -2$ in the case of linear vibronic coupling. [c] Calculated with $Q_\tau = 2\sqrt{2}R_{tr}(\theta - 54.7356°)(\pi/180)$. [d] $r_\tau = Q_\tau^{m}/Q_\tau^{s}$; $r_\tau = -2$ in the case of linear vibronic coupling. [e] Calculated with $Q_\theta = 2(dR_{ax}^{rh} - dR_{eq}^{rh})/\sqrt{3}$; $dR_{ax}^{rh} = R_{ax}^{rh} - R_{av}^{rh}$; $dR_{eq}^{rh} = R_{eq}^{rh} - R_{av}^{rh}$; $R_{av}^{rh} = (2R_{eq}^{rh} + R_{ax}^{rh})/3$; $Q_\zeta = |2R_{av}^{rh}(\alpha - 90°)(\pi/180)|\mathrm{sign}(V_\tau)$. [f] $r_\epsilon' = Q_\theta^{m'}/Q_\theta^{s}$; $r_\epsilon' = 1$ in the case of linear vibronic coupling; $r_\tau' = Q_\zeta^{m}/Q_\tau^{m}$; $r_\tau' = 3/2$ in the case of linear vibronic coupling.

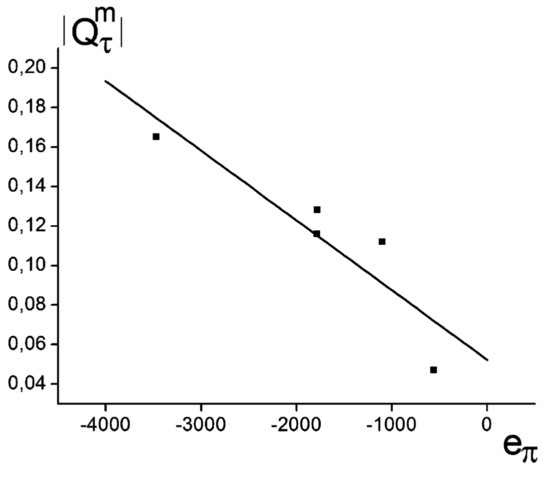

Figure 6. Correlation between the trigonal distortion $|Q_\tau^{m}|$ and the π boding energy e_π. Negative values of e_π imply dominating metal−ligand π-back-bonding for the $[M(CN)_6]^{3-}$ complexes: $e_\pi = -556, -1101, -1783, -1779, -3470$ cm^{-1} (M = Ti^{III}, V^{III}, Mn^{III}, Fe^{III}, Mn^{II}). Corresponding σ antibonding energies e_σ are 6694, 6376, 8976, 9304, and 5415 cm^{-1}, respectively (the cubic ligand splitting $\Delta = 10Dq$ is given by $\Delta = 3e_\sigma - 4e_\pi$); Δ = 22 300, 23 500, 34 000, 34 950, and 30 000 cm^{-1}.[41] The line drawn corresponds to a least-squares fit: $|Q_\tau^{m}| = 0.0523 - 0.000\,035\,26e_\pi$; standard deviation 0.018.

scribed in section II (see Table 5 and Figure 7). From a comparison of the JT stabilization energies it follows that the D_{3d} stationary points are deepest in energy, followed by those of D_{2h} and D_{4h} symmetry; a D_{4h} structure is obtained as the lowest energy minimum for $[Ti(CN)_6]^{3-}$. A good correlation between $E_{JT}(D_{3d})$ and the negative e_π value of each complex is obtained (Figure 8), in agreement with the V_τ vs e_π expression obtained with the angular overlap model:[43,44]

$$V_\tau = e_\pi/R \tag{32}$$

In Table 5 we compare results from the linear and quadratic approximations to the $T_g\otimes(\epsilon_g+\tau_{2g})$ JT coupling. All essential features, the order and magnitude of the stabilization, and structural distortions are correctly reproduced in the simple linear approximation. There are only small contributions from quadratic terms for the stationary points of D_{4h} and D_{2h} symmetry (see Table 4; r_ϵ and r_τ). Only in the case of the D_{3d} minima are the deviations of $r_\tau = Q_\tau^{m}/Q_\tau^{s}$ from the value for linear coupling ($r_\tau = -2$) large (see Table 4b). The use of the quadratic $T_g\otimes(\epsilon_g+\tau_{2g})$ JT coupling model is recommended here.

The parameters of Table 5 allow us to judge the vibronic coupling strength λ due to the ϵ_g and τ_{2g} vibrations, defined by the equations

$$\lambda_{\epsilon} = E_{\mathrm{JT}}(D_{4h})/\hbar\omega_{\epsilon} \tag{33}$$

$$\lambda_{\tau} = 2E_{\mathrm{JT}}(D_{4h})/3\hbar\omega_{\tau} \tag{34}$$

The values of λ_{ϵ} and λ_{τ} in Table 5 show that vibronic coupling with the ϵ_g modes is weak for all complexes. A weak vibronic coupling with the τ_{2g} mode is also obtained for $[\mathrm{Ti(CN)_6}]^{3-}$ and $[\mathrm{V(CN)_6}]^{3-}$. However, for $[\mathrm{Mn(CN)_6}]^{4-}$ and $[\mathrm{Cr(CN)_6}]^{4-}$, a strong vibronic coupling with the τ_{2g} mode is predicted. $[\mathrm{Fe(CN)_6}]^{3-}$ and $[\mathrm{Mn(CN)_6}]^{3-}$ represent intermediate cases (values of λ_{τ} are close to 1; see Table 5). For these ions, spin−orbit coupling is comparable with the $\mathrm{T_g}\otimes\tau_{2g}$ JT coupling. This will be analyzed in section IVc.

So far, we have focused on energies and geometries of stationary points on the ground-state potential energy surface. The parameters in Table 5 can also be used to assign the extrema of D_{4h}, D_{3d}, and D_{2h} symmetry to minima or saddle points. Starting from the ϵ_g and τ_{2g} force constants (K_{ϵ} and K_{τ}), we note that their values are modified by second-order vibronic coupling (see Table 3). Numerical values of the force constants for the diagonal (noninteracting) modes are given in Table 6a, where K_{ϵ} and K_{τ} for each complex, as well as their changes, are presented. In agreement with the small values of L_{ϵ}, these changes are negligible for the ϵ_g stretching mode (≤4% in the case of α_{1g} and β_{1g} (D_{4h})), except for $\mathrm{Fe^{III}}$ (±12%), and α_{1g} (1) and β_{1g} (D_{2h}). In contrast, for vibrations arising from the τ_{2g} bending modes, the changes of the force constants can be very large (120%, negative sign for $[\mathrm{Mn(CN)_6}]^{3-}$); these force constants are affected by L_{τ} (for D_{4h}), by X_{τ} (for D_{3d}), and by combinations of L_{τ} and X_{τ} (for D_{2h}; see Table 3). However, second-order vibronic coupling and the underlying forces are not large enough to change the sign of K_{τ} and to induce instability. Only in the case of $[\mathrm{Mn(CN)_6}]^{3-}$ is a large and negative value of L_{τ} calculated to lead to a negative force constant and instability along β_{2g} (τ_{2g}, Q_{ζ}) at the D_{4h} stationary point.

In addition to the diagonal changes of the force field due to the ϵ_g and τ_{2g} vibrations, vibronic mixing between the electronic states, induced by distortions away from the D_{4h}, D_{3d}, and D_{2h} stationary points, can cause dramatic changes, as shown by numerical calculations of the Hessian (see Table 6b, for the negative Hessian eigenvalues). A number of zero such eigenvalues indicates an absolute minimum. This is shown to be the case in D_{4h} for $[\mathrm{Ti(CN)_6}]^{3-}$ and in D_{3d} for M = $\mathrm{V^{III}}$, $\mathrm{Mn^{III}}$, $\mathrm{Fe^{III}}$, $\mathrm{Cr^{II}}$, $\mathrm{Mn^{II}}$. With the exception of M = $\mathrm{Ti^{III}}$, D_{3d} is the preferred geometry and D_{4h} extrema are found to be instable

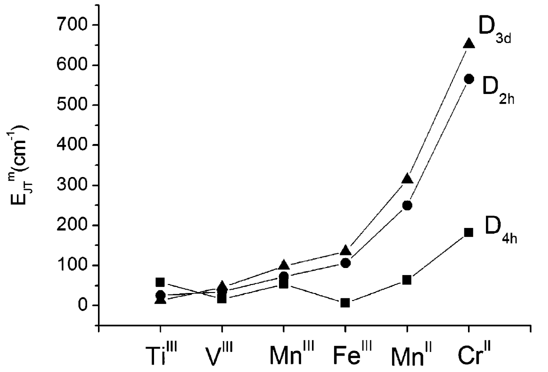

Figure 7. JT stabilization energies in hexacyanometalates of the 3d series in orbitally degenerate octahedral ground states in their D_{4h}, D_{3d}, and D_{2h} minima of the ground-state potential energy surface.

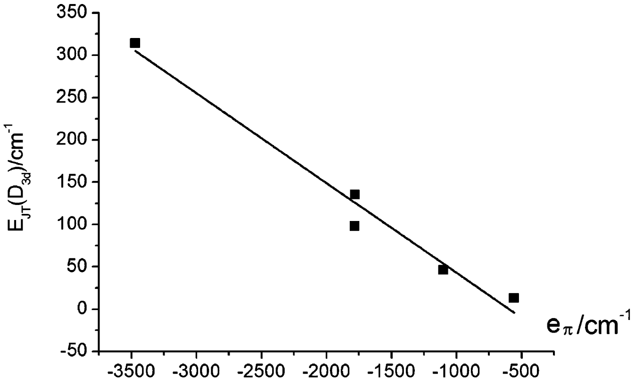

Figure 8. Correlation between the JT stabilization energies for the deepest minima of D_{3d} symmetry ($[\mathrm{V(CN)_6}]^{3-}$, $[\mathrm{Mn(CN)_6}]^{3-}$, $[\mathrm{Fe(CN)_6}]^{3-}$, $[\mathrm{Mn(CN)_6}]^{4-}$, $[\mathrm{Cr(CN)_6}]^{4-}$ in the order of increasing $E_{\mathrm{JT}}(D_{3d})$ energy) and the value of the parameter e_{π} dominated by π-back-bonding. $E_{\mathrm{JT}}(D_{3d}) = -0.106e_{\pi} - 62.92$, with a standard deviation of 18.08 and a correlation coefficient of −0.9881.

TABLE 5: Vibronic Couling Parameters of the Quadratic and Linear[a] $\mathbf{T_g\otimes(\epsilon_g+\tau_{2g})}$ JT Problem in 3d Hexacyanometalates in Orbitally Degenerate $\mathbf{T_g = {}^2T_{2g}\ (t_{2g}^1,\ t_{2g}^5)}$ or $\mathbf{{}^3T_{1g}\ (t_{2g}^2,\ t_{2g}^4)}$ Ground States, as Deduced from DFT as Well as JT Stabilization Energies for the $\boldsymbol{D_{4h}}$, $\boldsymbol{D_{3d}}$, and $\boldsymbol{D_{2h}}$ Stationary Points and Vibronic Coupling Strengths, $\boldsymbol{\lambda = 2E_{JT}/(n_{\Gamma}h\nu_{\Gamma})}$, for the $\mathbf{T_g\otimes\epsilon_g}$ ($\boldsymbol{\Gamma = \epsilon_g}$, $\boldsymbol{n_{\Gamma} = 2}$) and $\mathbf{T_g\otimes\tau_{2g}}$ ($\boldsymbol{\Gamma = \tau_{2g}}$, $\boldsymbol{n_{\Gamma} = 3}$) Jahn−Teller Problems

	complex					
	$[\mathrm{Ti(CN)_6}^{3-}]_{\mathrm{solv}}$	$[\mathrm{V(CN)_6}^{3-}]_{\mathrm{solv}}$	$[\mathrm{Mn(CN)_6}^{3-}]_{\mathrm{solv}}$	$[\mathrm{Fe(CN)_6}^{3-}]_{\mathrm{solv}}$	$[\mathrm{Cr(CN)_6}^{4-}]_{\mathrm{solv}}$	$[\mathrm{Mn(CN)_6}^{4-}]_{\mathrm{solv}}$
V_{ϵ} (cm^{-1}/Å)	3256 [3222]	−1661 [−1630]	3696 [3649]	−855 [−808]	7709 [7773]	−3918 [−3918]
L_{e} (cm^{-1}/Å^2)	1895	3134	3283	8235	−2714	0
K_{ϵ} (cm^{-1}/Å^2)	89063 [90010]	81478 [83045]	124758 [126400]	65882 [70000]	165545 [164188]	121173 [121173]
V_{τ} (cm^{-1}/Å)	−283 [−221]	408 [614]	−844 [−759]	1052 [1110]	−3572 [−3405]	1896 [1953]
X_{τ} (cm^{-1}/Å^2)	−1335	1839	−731	449	−917	344
K_{τ} (cm^{-1}/Å^2)	2251 [3140]	4887 [3661]	3858 [4345]	6069 [5770]	11820 [12432]	8099 [7870]
L_{τ} (cm^{-1}/Å^2)	−1158	4135	−4640	1584	−686	842
W (cm^{-1}/Å^2)	−2349	626	0	0	−659	0
$E_{\mathrm{JT}}(D_{4h})$ (cm^{-1})	58 [58]	16 [16]	53 [53]	5 [5]	182 [184]	63 [63]
$E_{\mathrm{JT}}(D_{3d})$ (cm^{-1})	13 [10]	46 [69]	98 [88]	135 [142]	652 [622]	314 [322]
$E_{\mathrm{JT}}(D_{2h})$ (cm^{-1})	25 [22]	35 [55]	72 [79]	106 [108]	565 [512]	250 [258]
$\hbar\omega_{\epsilon}{}^{b}$ (cm^{-1})	340	325	402	292	463	396
$\hbar\omega_{\tau}{}^{b}$ (cm^{-1})	50	76	72	93	124	106
$\lambda_{\epsilon} = E_{\mathrm{JT}}(D_{4h})/\hbar\omega_{\epsilon}$	0.171	0.049	0.132	0.017	0.393	0.160
$\lambda_{\tau} = 2[E_{\mathrm{JT}}(D_{3d})]/(3\hbar\omega_{\tau})$	0.178	0.399	0.905	0.965	3.519	1.971

[a] Given in brackets. [b] Calculated from the values of $K = K_{\epsilon}$, K_{τ} (in cm^{-1}/Å^2) and the equation $\hbar\omega = 1302.83(G{\cdot}K/50\,350)^{1/2}$. G is the diagonal element of the $\mathbf{G}$ matrix given by $G_{\epsilon} = 1/(m_{\mathrm{C}} + m_{\mathrm{N}}) = 1/26$; $G_{\tau} = 4/(m_{\mathrm{C}} + m_{\mathrm{N}})R_{\mathrm{tr}}^2$, m_{C} and m_{N} are the atomic masses of C and N, and R_{tr} = the distance from Table 4b. A DFT calculation of $\hbar\omega_{\epsilon}$ and $\hbar\omega_{\tau}$ for $[\mathrm{Cr(CN)_6}^{3-}]_{\mathrm{solv}}$ yields values of 315 and 78 cm^{-1}, respectively; the experimental value for $\hbar\omega_{\epsilon}$ is 339 cm^{-1}.

TABLE 6: (a) Normal Mode Force Constants and Their Changes[a] in Comparison with the Octahedral Values K_ϵ and K_τ (Noninteracting Modes) for the D_{4h}, D_{3d}, and D_{2h} Stationary Points on the $T_g \otimes (\epsilon_g + \tau_{2g})$ Ground-State Potential Energy Surface and (b) Eigenvalues (in cm^{-1}/Å^2) and Eigenvectors of the Hessian, Corresponding to Distortion Modes, Which Contribute to the Eventual Configurational Instabilities at the D_{4h}, D_{3d} ,and D_{2h} Stationary Points of M(CN)$_6$ Complexes[b]

sym mode[c]	Ti^{III}	V^{III}	Mn^{III}	Fe^{III}	Cr^{II}	Mn^{II}
(a) Normal Mode Force Constants						
O_h						
ϵ_g; K_ϵ	89063	81478	124758	65882	165545	121173
τ_{2g}: K_τ	2251	4887	3858	6069	11820	8099
D_{4h}						
$\alpha_{1g}(\epsilon_g)^d$	90958 (**2**)	84612 (**4**)	128042 (**3**)	74118 (**12**)	162831 (**−2**)	121173 (**0**)
$\beta_{1g}(\epsilon_g)^d$	87168 (**−2**)	78344 (**−4**)	121475 (**−3**)	57647 (**−12**)	168259 (**2**)	121173 (**0**)
$\beta_{2g}(\tau_{2g})^d$	1093 (**−51**)	9022 (**85**)	−782 (**−120**)	7653 (**26**)	11134 (**−6**)	8941 (**10**)
$\epsilon_g(\tau_{2g})^d$	2830 (**25**)	2820 (**−42**)	6178 (**60**)	5277 (**−13**)	12164 (**3**)	7678 (**−5**)
D_{3d}						
$\epsilon_g(\epsilon_g)^d$	89063 (**0**)	81478 (**0**)	124758 (**0**)	65882 (**0**)	165545 (**0**)	121173 (**0**)
$\alpha_{1g}(\tau_{2g})^d$	4030 (**79**)	2434 (**−50**)	4833 (**25**)	5470 (**−10**)	13044 (**10**)	7640 (**−6**)
$\epsilon_g(\tau_{2g})^d$	1361 (**−39**)	6113 (**25**)	3370 (**−13**)	6369 (**5**)	11209 (**−5**)	8328 (**3**)
D_{2h}						
$\beta_{1g}(\epsilon_g)^d$	90010 (**1**)	83045 (**2**)	126400 (**1**)	70000 (**6**)	164188 (**−1**)	121173 (**0**)
$\beta_{2g}(\tau_{2g})^d$	3296 (**46**)	4081 (**−16**)	3429 (**−11**)	6016 (**−1**)	12566 (**6**)	7966 (**−2**)
$\beta_{3g}(\tau_{2g})^d$	627 (**−72**)	7760 (**59**)	1967 (**−49**)	6915 (**14**)	10732 (**−9**)	8653 (**7**)
$\alpha_{1g}(1)(\epsilon_g,\tau_{2g})^d$	88180 (**−1**)	79916 (**−2**)	123117 (**−1**)	61765 (**−6**)	166905 (**1**)	121173 (**0**)
$\alpha_{1g}(2)(\epsilon_g,\tau_{2g})^d$	2765 (**23**)	2814 (**−42**)	6178 (**60**)	5277 (**−13**)	12161 (**3**)	7678 (**−5**)
(b) Eigenvalues and Eigenvectors						
D_{4h}						
$\epsilon_g(\tau_{2g})$	[1351]	[−1680]	[−4814]	[−126721]	[−35580]	[−29733]
	2158	−4339	−2840	−152900	−33670	−30150
Q_θ	0.00, 0.00	0.00, 0.00	0.00, 0.00	0.00, 0.00	0.00, 0.00	0.00, 0.00
Q_ϵ	0.00, 0.00	0.00, 0.00	0.00, 0.00	0.00, 0.00	0.00, 0.00	0.00, 0.00
Q_ξ	−0.71, 0.71	−0.71, 0.71	−0.70, −0.71	0.71, −0.71	0.71, 0.71	0.71, 0.71
Q_η	0.71, 0.71	0.71, 0.71	−0.72, 0.70	−0.71, −0.71	−0.71, 0.71	−0.71, 0.71
Q_ζ	0.00, 0.00	0.00, 0.00	0.00, 0.00	0.00, 0.00	0.00, 0.00	0.00, 0.00
	(0)[e]	(2)[e]	(3)[e]	(2)[e]	(2)[e]	(2)[e]
D_{3d}						
$[\epsilon_g(\epsilon_g)/\epsilon_g(\tau_{2g})]$	[−61521]	[1589]	[2017]	[3978]	[7052]	[4927]
	−232780	2821	3308	3658	5720	5000
Q_θ	0.81, −0.58	0.04, −0.09	−0.01, 0.02	0.03, −0.01	0.07, −0.05	−0.03, −0.06
Q_ϵ	−0.58, −0.81	0.09, 0.04	−0.02, −0.01	−0.01, −0.03	−0.05, −0.07	−0.06, 0.03
Q_ξ	−0.06, −0.03	0.47, 0.66	−0.51, −0.64	−0.65, −0.49	−0.72, −0.37	−0.41, 0.70
Q_η	0.01, 0.07	−0.81, 0.08	0.81, −0.12	−0.10, 0.81	0.04, 0.81	0.81, 0.01
Q_ζ	0.06, −0.04	0.34, −0.74	−0.30, 0.76	0.75 ,−0.32	0.68, −0.44	−0.40, −0.71
	(2)[e]	(0)[e]	(0)[e]	(0)[e]	(0)[e]	(0)[e]
D_{2h}						
$\beta_{1g}(\epsilon_g)$	[−134156]	[20844]	[69254]	[62871]	[124262]	[95233]
	−277250	50723	39870	67719	120700	96580
Q_θ	0.00	0.00	0.00	0.00	0.00	0.00
Q_ϵ	1.00	1.00	1.00	1.00	1.00	1.00
Q_ξ	0.00	0.00	0.00	0.00	0.00	0.00
Q_η	0.00	0.00	0.00	0.00	0.00	0.00
Q_ζ	0.00	0.00	0.00	0.00	0.00	0.00
β_{2g} (τ_{2g})	[967]	[−717]	[−1482]	[−5539]	[−7102]	[−5243]
	2560	−1712	−4830	−3779	−4990	−5080
Q_θ	0.00	0.00	0.00	0.00	0.00	0.00
Q_ϵ	0.00	0.00	0.00	0.00	0.00	0.00
Q_ξ	0.71	0.71	0.71	0.71	0.71	0.71
Q_η	0.71	0.71	0.71	0.71	0.71	0.71
Q_ζ	0.00	0.00	0.00	0.00	0.00	0.00
	(1)[e]	(1)[e]	(1)[e]	(1)[e]	(1)[e]	(1)[e]

[a] Changes (in percentages), with respect to the corresponding values of K_ϵ and K_τ, are given in parenthesis in boldface type. [b] Entries in brackets are based on the linear $T_g \otimes (\epsilon_g + \tau_{2g})$ vibronic coupling model (eqs 3 and 5−9); the other entries are obtained by a numerical calculation of the Hessian at the D_{4h}, D_{3d}, and D_{2h} equilibrium points, using eq 1 and vibronic coupling parameters from Table 5. [c] The origin of each mode from the corresponding O_h normal vibration is given in parentheses. [d] Calculated from the expressions in Table 3 and vibronic coupling parameters from Table 5. [e] The total number of negative eigenvalues of the Hessian is given in parentheses. Legend: (0) minimum; (1) first-order saddle point, a reactive transition state; (2) second-order saddle point; (3) exotic type of instability (monkey saddle). The eigenvalue not listed for [Mn(CN)$_6$]$^{3-}$ is that of $\beta_{2g}(\tau_{2g})$ (-782 cm^{-1}/Å^2, see part a).

for all these cases. The latter is a rare situation of a second-order saddle point for this geometry (two negative Hessian eigenvalues for the ϵ_g (τ_{2g}) mode). An extraordinary case is [Mn(CN)$_6$]$^{3-}$, where the eigenvalues due to all three components of the τ_{2g} mode (ϵ_g and β_{2g}) are negative. Vibronic mixing is responsible for this in the case of ϵ_g, and a diagonal modification by second-order JT forces is the origin in the case of β_{2g}. A D_{3d} saddle point with an instability, caused by the ϵ_g stretching

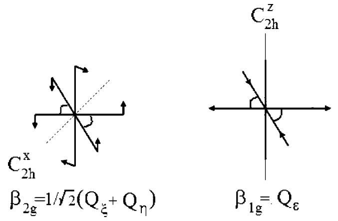

Figure 9. Vibrations β_{2g} (component of τ_{2g}) and β_{1g} (component of ϵ_g), which lead to a mixing between the B_{2g} ground state of the D_{2h} minimum with the A_{1g} and B_{3g} states, respectively. The β_{2g} mode drives the system into a D_{3d}^{xyz} minimum via a continuous line of C_{2h}^{x} structures, while the β_{1g} mode leads to a D_{4h}^{x} stationary point via a C_{2h}^{z} distortion path.

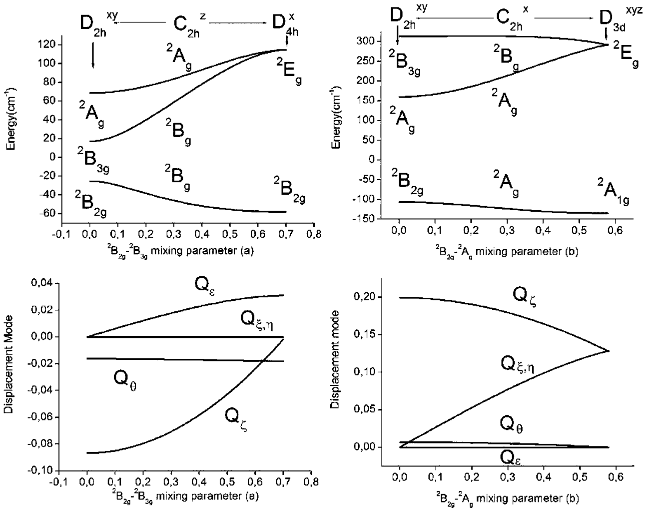

Figure 10. Distortion paths due to $B_{2g}\otimes\beta_{1g}\otimes B_{3g}$ ($[Ti(CN)_6]^{3-}$, left) and $B_{2g}\otimes\beta_{2g}\otimes A_g$ ($[Fe(CN)_6]^{3-}$, right) vibronic interactions starting from the D_{2h}^{xy} stationary point expressed in terms of the single electronic mixing parameters (a) and (b), respectively. The top curves represent the electronic energies of the components of the $^2T_{2g}$ ground state. The bottom curves display the concomitant changes of the components of the five $\epsilon_g + \tau_{2g}$ vibrational modes. The data have been obtained by varying (a) and (b), calculating Q_θ, Q_ϵ, Q_ξ, Q_η, and Q_ζ, using the stationary conditions (method of Öpik and Price[29]), and solving the secular equation with these values. Vibronic coupling parameters used to construct the diagram are those for $[Ti(CN)_6]^{3-}$ (left) and $[Fe(CN)_6]^{3-}$ (right) (Table 5). As the method of Öpik and Price is, in a strict sense, only applicable at special points of high symmetry (for which electronic eigenfunctions are known by symmetry; initial and final points on the abscissa on each diagram), intermediate points should be viewed with care, and these serve only as a tool for interpolation between the D_{2h} and D_{4h} (left) and D_{2h} and D_{3d} (right) limiting cases.

mode, is calculated for $[Ti(CN)_6]^{3-}$ with a D_{4h} stable minimum. That is, the vibration that drives the systems into the absolute minimum, i.e., $\epsilon_g(O_h)$ for $[Ti(CN)_6]^{3-}$ (D_{4h}) and τ_{2g} for M = V^{III}, Mn^{III}, Fe^{III}, Cr^{II}, Mn^{II} (D_{3d}), causes instability in the alternative symmetry, D_{3d} and D_{4h}, respectively. The β_{1g} (ϵ_g) mode for $[Ti^{III}(CN)_6]^{3-}$ and the β_{2g} (τ_{2g}) mode for all other complexes are the distortion modes responsible for the instabilities at the D_{2h} stationary points (Figure 9).

One negative root of the Hessian (reactive transition state) is obtained in all these complexes. In Figure 10, we visualize the changes of the electronic energy and the concomitant changes of the Q_θ, Q_ϵ, Q_ξ, Q_η, and Q_ζ nuclear coordinates with a single variable parameter, which describes the mixing of the ground state B_{2g} with B_{3g} ($[Ti(CN)_6]^{3-}$, left) and A_g excited states ($[Fe(CN)_6]^{3-}$, right) by virtue of the β_{1g} (ϵ_g) and β_{2g} (τ_{2g}) stretching and bending vibrations. Starting from the D_{2h}^{xy} stationary point, β_{1g} (ϵ_g) and β_{2g} (τ_{2g}) distortions drive the system via a continuous distortion path of C_{2h}^{z} and C_{2h}^{x} symmetry into the D_{4h}^{x} (or D_{4h}^{y}, depending on the sign of β_{1g} (ϵ_g)) and D_{3d}^{xyz} absolute minima for $[Ti(CN)_6]^{3-}$ and $[Fe(CN)_6]^{3-}$, respectively.

The linear vibronic coupling model (Table 6b, entries given in brackets) is able to reproduce the topology of the ground-state potential energy surface due to $T_g\otimes(\epsilon_g+\tau_{2g})$ vibronic coupling. With one exception ($[Mn(CN)_6]^{3-}$; see Table 6a) all minima and saddle points are correctly predicted. It appears from our DFT-based analysis that the instabilities at the D_{4h}, D_{3d}, and D_{2h} stationary points on the ground-state potential energy surface of the complexes discussed here are mainly due to vibronic mixing between electronic states, and this is correctly described at the level of the linear JT coupling.

b. Effect of Configurational Interaction (CI) on the Ground-State $T_g\otimes(\epsilon_g+\tau_{2g})$ JT Coupling. We have considered $^2T_{2g}$ and $^3T_{1g}$ ground states and focus on a single t_{2g}^{n} configuration. Strictly, this is only valid for $t_{2g}^{1}(Ti^{III})$, and it is an approximation for d^5 and the $d^{2,4}$ metal ions. The $^2T_{2g}$ and $^3T_{1g}$ ground states of $[Fe(CN)_6]^{3-}$ and $[Mn(CN)_6]^{3-}$ are mixtures of as much as 10 (T_{2g}) and 7 (T_{1g}) species of the same symmetry, which differ in their electron configurations of the MOs of d character. These terms mix with each other via interelectronic repulsion (CI) and split because of excited-state JT coupling, due to π-type vibronic mixing (via the τ_{2g} mode, splitting of the t_{2g} orbitals). For $[Fe(CN)_6]^{3-}$ and $[Mn(CN)_6]^{3-}$ (strong ligand field), the t_{2g}^{5} and t_{2g}^{4} configurations are expected to dominate the ground-state wavefunction but the excited-state configurations might still be important for the ground-state vibronic coupling. Unfortunately, there are no DFT methods for the explicit geometry optimization of electronic states of multiconfigurational character. In DFT, one assumes that a single configuration dominates the electronic and geometric structures. To trace the effect of CI on the ground-state JT effect of these ions, we resort to ligand field theory (LFT) and focus on the D_{3d} minima of the ground-state potential energy surface. For some of the complexes studied here, approximate values of $10Dq$, B, and C are known (Table 7).[41] They have been used in a CI calculation of the ground state $^2T_{2g}$ (Fe^{III}, Mn^{II}) and $^3T_{1g}$ (V^{III}, Mn^{III}) terms. From the known values of the trigonal distortion angle θ, the energy E_{FC}^{m}, and $10Dq$, we deduce the angular overlap parameters from one-electron calculations and then switch to a many-electron CI treatment. The ground-state splitting which results from such a calculation is E_{FC}^{CI}. Since the energies E_{FC} and E_{JT} are interrelated (see section II), we can use eq 35 to obtain an approximation of the JT stabilization energy.

$$E_{JT}^{CI} = E_{JT}^{m}(E_{FC}^{CI}/E_{FC}^{m}) \tag{35}$$

The results in Table 7 show that CI mixing is essential and leads to an enhancement of the ground-state splitting and an increase of the magnitude of E_{FC} by about a factor of 2 for $[Fe(CN)_6]^{3-}$ and $[V(CN)_6]^{3-}$. For the latter complex the effect of CI is opposite to complexes with π-donor ligands (VF_6^{3-}), where it was found with structural and spectroscopic data that CI reduces the $^3T_1$ ground-state JT coupling.[42]

c. Effect of the Combination of the $T_g\otimes(\epsilon_g+\tau_{2g})$ JT and Spin−Orbit Coupling on the Ground-State Potential Energy Surface. Spin−orbit coupling (quantified by the spin−orbit coupling constant ζ) leads to a first-order splitting of the octahedral $^2T_{2g}$ and $^3T_{1g}$ ground states with the following energies of the twofold (Γ_7) and fourfold (Γ_8) degenerate states (for $^2T_{2g}$ $d^1(d^5)$) and of the nondegenerate (A_1) and threefold (T_1) and fivefold degenerate E, T_2 states (accidental degeneracy) for ($^3T_{1g}$ d^2 (d^4)) ($\zeta > 0$):

$$[\mathrm{Ti(CN)_6}]^{3-}\ (\mathrm{d}^1){:}\ \Gamma_8[-(1/2)\zeta] < \Gamma_7[\zeta] \tag{36}$$

$$[\mathrm{Fe(CN)_6}]^{3-},\ \mathrm{Mn(CN)_6}^{4-}\ (\mathrm{d}^5){:}\ \Gamma_7[-\zeta] < \Gamma_8[(1/2)\zeta] \tag{37}$$

$$[\mathrm{V(CN)_6}]^{3-}\ (\mathrm{d}^2){:}\ (\mathrm{T_2,E})[-(1/2)\zeta] < \mathrm{T_1}[(1/2)\zeta] < \mathrm{A_1}[\zeta] \tag{38}$$

$$[\mathrm{Mn(CN)_6}]^{3-},\ [\mathrm{Cr(CN)_6}]^{4-}\ (\mathrm{d}^4){:}\ \mathrm{A_1}[-\zeta] < \mathrm{T_1}[-(1/2)\zeta] < (\mathrm{T_2,E})[(1/2)\zeta] \tag{39}$$

While spin−orbit coupling lifts the orbital degeneracy and, therefore, opposes the JT forces for $[\mathrm{Fe(CN)_6}]^{3-}$, $[\mathrm{Mn(CN)_6}]^{4-}$, $[\mathrm{Mn(CN)_6}]^{3-}$, and $[\mathrm{Cr(CN)_6}]^{4-}$, this is not the case for $\mathrm{Ti(CN)_6}]^{3-}$ and $[\mathrm{V(CN)_6}]^{3-}$, where the ground states remain fourfold and (accidentally) fivefold degenerate, respectively. Values of ζ for these ions (Table 7) from relativistic two-component (ZORA) DFT calculations (reduced by metal−ligand covalency[45,46]) have been used to calculate the stabilization by spin−orbit coupling on the ground-state energy (E_{SOC}, Table 7). On the basis of the comparison between E_{SOC} and $E_{\mathrm{JT}}{}^{\mathrm{m}}$, we can conclude that spin−orbit coupling and JT coupling are of comparable magnitude, except for $\mathrm{Mn^{II}}$ and $\mathrm{Cr^{II}}$ (not listed). In Figure 11 we present contour plot diagrams for $[\mathrm{Mn(CN)_6}]^{3-}$ and $[\mathrm{Fe(CN)_6}]^{3-}$ with trigonal distortion modes and take Q_ζ and $Q_\xi = Q_\eta$ as independent variables: i.e., the subspace of all distortions compatible with the symmetry $C_{2h}{}^{x}$ (see Figure 10). In the upper part of Figure 11 spin−orbit coupling is set to zero, and the D_{3d} minima and D_{2h} saddle points are easily recognizable. As seen from the lower part of Figure 11, the inclusion of spin−orbit coupling leads to specific changes. The JT stabilization ($E_{\mathrm{JT}}{}^{\mathrm{m}} = 98$, $\zeta = 0$) vanishes ($E_{\mathrm{JT}}{}^{\mathrm{m}} = 0$, $\zeta = 284$) for $[\mathrm{Mn(CN)_6}]^{3-}$, and it becomes strongly reduced for $[\mathrm{Fe(CN)_6}]^{3-}$ (from $E_{\mathrm{JT}}{}^{\mathrm{m}} = 135\ \mathrm{cm^{-1}}$, $\zeta = 0$ to $E_{\mathrm{JT}}{}^{\mathrm{m}} = 12\ \mathrm{cm^{-1}}$, $\zeta = 347\ \mathrm{cm^{-1}}$). $E_{\mathrm{JT}}{}^{\mathrm{CI}}$ is nonzero for $[\mathrm{Fe(CN)_6}]^{3-}$, but it is sufficiently reduced by spin−orbit coupling to suppress the JT coupling via the zero-point energy of the τ_{2g} vibration.

Contour plot diagrams for $[\mathrm{Ti(CN)_6}]^{3-}$ and $[\mathrm{V(CN)_6}]^{3-}$ are presented in Figure 12. The orbital degeneracy is not lifted by spin−orbit coupling, and the effect of spin−orbit coupling on the ground-state potential energy surface is less pronounced than with $[\mathrm{Mn(CN)_6}]^{3-}$ and $[\mathrm{Fe(CN)_6}]^{3-}$. Nevertheless, there is a significant reduction of $E_{\mathrm{JT}}{}^{\mathrm{m}}$ (from $E_{\mathrm{JT}}{}^{\mathrm{m}} = 58\ \mathrm{cm^{-1}}$, $\zeta = 0$ to $E_{\mathrm{JT}}{}^{\mathrm{m}} = 24\ \mathrm{cm^{-1}}$, $\zeta = 147\ \mathrm{cm^{-1}}$ for $[\mathrm{Ti(CN)_6}]^{3-}$; from $E_{\mathrm{JT}}{}^{\mathrm{m}} = 46\ \mathrm{cm^{-1}}$, $\zeta = 0$ to $E_{\mathrm{JT}}{}^{\mathrm{m}} = 31\ \mathrm{cm^{-1}}$, $\zeta = 190\ \mathrm{cm^{-1}}$ for $[\mathrm{V(CN)_6}]^{3-}$). Our results show that JT coupling is larger than spin−orbit coupling for $[\mathrm{Mn(CN)_6}]^{4-}$ ($E_{\mathrm{JT}}{}^{\mathrm{m}}(D_{3d}) = 314\ \mathrm{cm^{-1}}$, $E_{\mathrm{SOC}} = 243\ \mathrm{cm^{-1}}$) and much larger for $[\mathrm{Cr(CN)_6}]^{4-}$ ($E_{\mathrm{JT}}{}^{\mathrm{m}}(D_{3d}) = 652\ \mathrm{cm^{-1}}$, $E_{\mathrm{SOC}} = 193\ \mathrm{cm^{-1}}$). Therefore, for these complexes and dynamic JT coupling, it is expected that spin−orbit coupling will be strongly reduced by vibronic coupling (Ham effect; see section Vb.2). JT coupling and spin−orbit coupling counteract in the case of $[\mathrm{Mn(CN)_6}]^{3-}$ and $[\mathrm{Fe(CN)_6}]^{3-}$ to an extent to nearly suppress minima on the ground-state potential energy

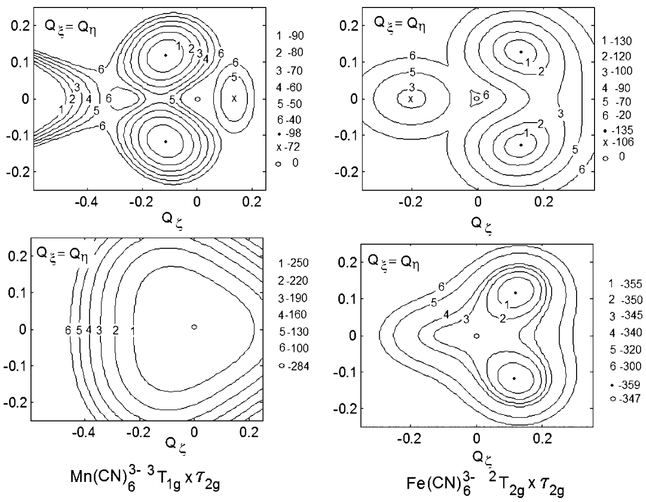

Figure 11. Contour plot diagrams of $[\mathrm{Fe(CN)_6}]^{3-}$ (top right, $\zeta = 0$; bottom right, $\zeta = 347\ \mathrm{cm^{-1}}$) and $[\mathrm{Mn(CN)_6}]^{3-}$ (top left, $\zeta = 0$; bottom left, $\zeta = 284\ \mathrm{cm^{-1}}$). D_{2h} and D_{3d} minima are indicated by × and •, respectively; vibronic coupling parameters used to construct the plot are those given in Table 5 (quadratic JT coupling).

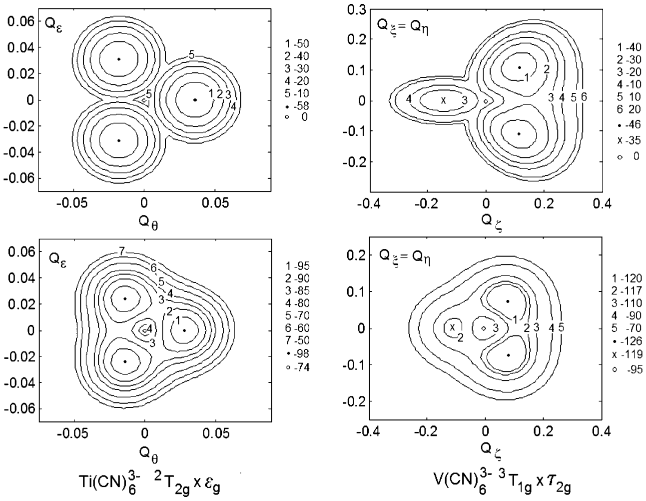

Figure 12. Contour plot diagrams of $[\mathrm{V(CN)_6}]^{3-}$ (top right, $\zeta = 0$; bottom right, $\zeta = 95\ \mathrm{cm^{-1}}$; D_{2h} and D_{3d} minima are indicated by × and •, respectively) and $[\mathrm{Ti(CN)_6}]^{3-}$ (top left, $\zeta = 0$; bottom left, $\zeta = 74\ \mathrm{cm^{-1}}$; D_{4h} minima are indicated by •). Vibronic coupling parameters used to construct the plots are those given in Table 5 (quadratic JT coupling).

TABLE 7: Angular Overlap Model Parameters[a] and the Trigonal Angles (θ[b]) for CI Calculations of the Effect of Configurational Mixing on the JT Energies: $E_{\mathrm{FC}}{}^{\mathrm{m}}$ (JT Splitting) and E_{JT} (JT Stabilization Energy)[c]

complex	10*Dq*[d]	$E_{\mathrm{FC}}{}^{\mathrm{m}}$	$E_{\mathrm{FC}}{}^{\mathrm{CI}}$	θ	e_σ	e_π	E_{JT}	$E_{\mathrm{JT}}{}^{\mathrm{CI}}$	*B*[d]	*C*[d]	ζ[f]	E_{SOC}[e]
$[\mathrm{Ti(CN)_6}]^{3-}$	22300	31		54.30	6694	−556	13				147	74
$[\mathrm{V(CN)_6}]^{3-}$	23500	206	342	55.82	6376	−1101	46	74	375	2700	190	95
$[\mathrm{Mn(CN)_6}]^{3-}$	34000	265	397	53.53	8976	−1783	98	147	675	3120	284	284
$[\mathrm{Fe(CN)_6}]^{3-}$	34950	427	830	56.10	9304	−1779	135	262	720	3290	347	347
$[\mathrm{Mn(CN)_6}]^{4-}$	30000	969	1196	56.47	5415	−3470	314	387	425	1800	243	243

[a] Deduced from a fit of e_σ and e_π to the t_{2g} splitting ($E_{\mathrm{FC}}{}^{\mathrm{m}}$) and the value of 10Dq using the angles θ. [b] Values of θ correspond to the D_{3d} minima (see Table 4b). [c] E_{JT} values accounting for CI, $E_{\mathrm{JT}}{}^{\mathrm{CI}}$, are calculated using $E_{\mathrm{JT}}{}^{\mathrm{CI}} = E_{\mathrm{JT}}{}^{\mathrm{m}}(E_{\mathrm{FC}}{}^{\mathrm{CI}}/E_{\mathrm{FC}}{}^{\mathrm{m}})$. [d] From ref 41. [e] Calculated from the energy expression for states split from ${}^2\mathrm{T_{2g}}$ and ${}^3\mathrm{T_{1g}}$ due to spin−orbit coupling (ζ is defined to be positive in all cases). $\mathrm{Ti(CN)_6}^{3-}$: Γ_8, $-(1/2)\zeta$, Γ_7, ζ. $\mathrm{V(CN)_6}^{3-}$: ($\mathrm{T_2}$,E), $-(1/2)\zeta$; $\mathrm{T_1}$, $(1/2)\zeta$; $\mathrm{A_1}$, ζ. $\mathrm{Mn(CN)_6}^{3-}$: $\mathrm{A_1}$, $-\zeta$; $\mathrm{T_1}$, $-(1/2)\zeta$; ($\mathrm{T_2}$,E), $(1/2)\zeta$. $\mathrm{Fe(CN)_6}^{3-}$ and $\mathrm{Mn(CN)_6}^{4-}$: Γ_7, $-\zeta$; Γ_8, $(1/2)\zeta$. [f] Deduced from two-component relativistic (ZORA) calculations on the $\mathrm{M^{3+}}$ (Ti, 200 $\mathrm{cm^{-1}}$; V, 264 $\mathrm{cm^{-1}}$; Mn, 429 $\mathrm{cm^{-1}}$; Fe, 548 $\mathrm{cm^{-1}}$) and $\mathrm{M^{2+}}$ (Mn, 368 $\mathrm{cm^{-1}}$; Cr, 284 $\mathrm{cm^{-1}}$) ions after a proper reduction by covalency; the value of the spin−orbit coupling constant for $\mathrm{Cr^{II}}$ (not listed) is $\zeta = 193\ \mathrm{cm^{-1}}$.

TABLE 8: Comparison of Experimental and Computed Radial (ρ_ϵ) and Angular (ρ_τ) Distortions[a] from the Regular Octahedral Geometries of 3d Hexacyanometalate Complexes

		exptl		theor[b]		
complex	counterion	ρ_ϵ	ρ_τ	ρ_ϵ	ρ_τ	ref
$[Mn(CN)_6]^{3-}$	$3[N(PPh_3)_2]^+$	0.012(2)	0.148(6)	0.029	0.116	47
$[Mn(CN)_6]^{3-}$	$3K^+$	0.044(14)	0.040(40)	0.029	0.116	48a
$[Fe(CN)_6]^{3-}$	$3[N(PPh_3)_2]^+$	0.021(7)	0.202(20)	0.012	0.128	49
$[Fe(CN)_6]^{3-}$ [c]	$3K^+$	0.016(3)	0.088(7)	0.012	0.128	20
$[Fe(CN)_6]^{3-}$ [d]	$3K^+$	0.000(6)	0.103(20)	0.012	0.128	20
$[Co(CN)_6]^{3-}$	$3K^+$	0.040(11)	0.014(31)	0	0	48b
$[Cr(CN)_6]^{4-}$	$4Na^+$	0.029(6)	0.169(14)	0.047	0.182	50

[a] Calculated using $\rho_\epsilon = (\sum_{i=1}^{6}\Delta R_i^2)^{1/2}$, where $\Delta R_i = R_i - R_{av}$ and R_{av} is the average M−CN bond distance, and $\rho_\tau = R_{av}(\sum_{i=1}^{12}\Delta\alpha_i^2)^{1/2}$, where $\Delta\alpha_i = \pi(\alpha_i - 90)/180$ and α_i denotes the 12 *cis*-C−M−C bond angles in a hexacoordinate complex. [b] Calculated for the D_{4h} (ρ_ϵ) and D_{3d} (ρ_τ) minima of the ground-state potential energy surface. [c] Monoclinic form. [d] Orthorhombic form.

surface, calculated to be of D_{3d} symmetry. The JT coupling may still manifest itself on potential energy surfaces, which are very flat along distortional modes of τ_{2g} symmetry. These ions are expected to be susceptible to angular distortions.

V. Comparison with Experiment

a. Structural Data. Hexacyanometalates of the 3d metals are anionic species, and crystal and molecular structures of their compounds with alkali-metal ions have been reported.[20,47−50] The M(CN)$_6$ units are nearly octahedral, with small distortions in bond lengths and angles. To quantify these distortions and to facilitate comparison between the predicted and observed structures, we introduce JT radii for the ϵ_g and τ_{2g} modes, defined in eqs 40 and 41, and use reported bond lengths and

$$\rho_\epsilon = (Q_\theta^{\ 2} + Q_\epsilon^{\ 2})^{1/2} = (\sum_{i=1}^{6}\Delta R_i^{\ 2})^{1/2} \qquad (40)$$

$$\Delta R_i = R_i - R_{av}$$

$$\rho_\tau = (Q_\xi^{\ 2} + Q_\eta^{\ 2} + Q_\zeta^{\ 2})^{1/2} = R_{av}(\sum_{i=1}^{12}\Delta\alpha_i^{\ 2})^{1/2} \qquad (41)$$

$$\Delta\alpha_i = \pi(\alpha_i - 90)/180$$

angles to approximate their values. In eqs 40 and 41 R_{av} is the average M−CN distance, while α_i values give the 12 *cis*-C−M−C angles. In Table 8, values of ρ_ϵ and ρ_τ from X-ray diffraction data of $[Mn(CN)_6]^{3-}$, $[Fe(CN)_6]^{3-}$, and $[Cr(CN)_6]^{4-}$ are compared with those deduced from the D_{4h} (ρ_ϵ) and D_{3d} (ρ_τ) DFT geometry optimizations. There is good agreement between the orders of magnitude of ρ_ϵ and ρ_τ from DFT and experimental data. In agreement with the predicted larger JT coupling of the trigonal (τ_{2g}) compared with the tetragonal modes (ϵ_g), we obtain $\rho_\tau \gg \rho_\epsilon$. However, from a comparison of the ρ_ϵ and ρ_τ values of $[Fe(CN)_6]^{3-}$ (or $[Mn(CN)_6]^{3-}$) in crystal lattices with various counterions or from different crystal structural analyses (orthorhombic vs monoclinic), it follows that there is a significant matrix effect. This conclusion also emerges from the observed small distortions of the JT-inert $[Co(CN)_6]^{3-}$ complex.

b. The g Tensor Values and the Anisotropic Susceptibility of K$_3$[Fe(CN)$_6$]. *b.1. Static Strain along the τ_{2g} Distortions.* The electronic structure of $[Fe(CN)_6]^{3-}$ has been extensively studied, starting with the early work on the paramagnetic resonance of $[Fe(CN)_6]^{3-}$ and its theoretical interpretation.[13,14] In addition, magnetic susceptibility (χ) studies, including crystal anisotropies and crystal structures, have been reported.[15,18,21] Efforts to rationalize these data were based on the assumption of an orthorhombic symmetry with orthorhombic axes parallel to the three Fe−CN bond directions. A reasonable fit with three parameters (two crystal field energies, which define the splitting of the *xy*, *yz*, and *xz* orbitals (*A*(*xy*), *B*(*yz*), and *C*(*xz*), respectively; $A + B + C = 0$ and the spin−orbit coupling constant) could reproduce both the **g** tensors and the anisotropic susceptibility. However, the Mössbauer data of $[Fe(CN)_6]^{3-}$ [16,17,19] could not be explained. The room-temperature (295 K) crystal structures of K$_3$[Fe(CN)$_6$] in its monoclinic and orthorhombic forms have been determined with high precision.[20] As follows from the C−Fe−C angles (Table 9a; α_ξ, α_η, and α_ζ), $[Fe(CN)_6]^{3-}$ is found in a trigonally elongated geometry with the C_3 axis approximately parallel to the crystallographic axis (*a*), superimposed by an additional orthorhombic distortion. We have used the distortions to get an estimate of the geometric strain, described by $Q_\xi^{\ s}$, $Q_\eta^{\ s}$, and $Q_\zeta^{\ s}$ (see Table 9), and the vibronic coupling constants of $[Fe(CN)_6]^{3-}$ to approximate the strain matrix according to eq 21, to calculate the **g** and susceptibility tensors of $[Fe(CN)_6]^{3-}$ from a full LF calculation. With this matrix, we could not reproduce the sign of the magnetic anisotropy. Apparently, the geometry of $[Fe(CN)_6]^{3-}$ doped into K$_3$[Co(CN)$_6$] is not the same as that given by the room-temperature structure of K$_3$[Fe(CN)$_6$], and the latter may change going to lower temperatures. Here, probably a geometric distortion, dominated by a trigonal compression, takes place. This is compatible with the stabilization of a nondegenerate (JT stable) $^2A_{1g}$ ground state. If we adopt the values of $Q_\xi^{\ s}$, $Q_\eta^{\ s}$, and $Q_\zeta^{\ s}$, deduced from X-ray data of the two modifications, and change their sign, accurate computed anisotropic **g**-tensor components and low-temperature magnetic susceptibility are obtained. The results are given in Table 9a and plotted in Figure 13. Readjustment of the values of $-Q_\xi^{\ s}$, $-Q_\eta^{\ s}$, and $-Q_\zeta^{\ s}$ did not further strongly improve the agreement with experiment. From the data in Table 9b, the orientation of the principal axes of the **g** tensor with respect to the two sets of axes, the octahedral Fe−C bond directions, and the crystallographic *a*, *b*, and *c* axes also emerge. The orientations yield the (1,1,1) (0,−1,1) and (2,−1,−1) trigonal directions for g_1, g_2, and g_3. These orientations show that g_1, g_2, and g_3 are (within angles of 11, 8, and 17°) parallel to the (*a*), (*c*), and (*b*) crystal axes in the orthorhombic lattice. In the monoclinic form, the axis of g_1 is parallel to (*a*) but the directions of g_2 and g_3 interchange and become aligned along (*b*) and (*c*), respectively. This phenomenon has been described before.[17] There is a misfit between the directions of g_1 and χ_1 (both $\|a$, see the entries for (II) and (V) in Table 9b) and the orientation of g_1 reported in ref 13, where the crystal structure of K$_3$[Fe(CN)$_6$] was not known. In agreement with the susceptibility data, the magnetic anisotropies of $[Fe(CN)_6]^{3-}$ in the two crystallographic forms of K$_3$[Fe(CN)$_6$] are very similar and only compatible with a trigonally compressed geometry, as indicated by the JT coupling model. A change of the angle $\theta = 54.7350°$ by only 1° is large enough to account for the observed anisotropy of g and χ.

b.2. Dynamic Jahn−Teller Coupling. The τ_{2g} vibrational frequencies of $[Mn(CN)_6]^{3-}$ and $[Fe(CN)_6]^{3-}$ are comparable with the JT stabilization energies E_{JT} (D_{3d}). Therefore, dynamic JT coupling can take place. The $^2T_{2g}$ electronic state of $[Fe(CN)_6]^{3-}$ undergoes mixing with vibrational states, and this leads to a total vibronic state of the same symmetry. Spin−orbit coupling splits this $^2T_{2g}$ vibronic state into a Γ_7 ground

TABLE 9: (a) Geometric and g tensor Values for $[Fe(CN)_6]^{3-}$ in Its Orthorhombic and Monoclinic Forms Given by Experiment and Simulated with a Vibronic JT Coupling Model and (b) Directional Cosines of the Principal Axes of the g Tensor with Respect to the Octahedral Fe−C bond Directions (*x*, *y*, *z*) and the Crystallographic *a*, *b*, *c* (Orthorhombic Setting) As Deduced from Experiment (III) and Simulated (Best Fit of Geometric Parameters) for $[Fe(CN)_6]^{3-}$ in Its Orthorhombic (II) and Monoclinic (V) Forms

(a) Geometric and **g** Tensor Values

	orthorhombic[b]			monoclinic[c]	
	X-ray struct[20] (exptl) I	geom from a fit to **g** tensor values II	g_{exptl}[13] III	X-ray struct[20] (exptl) IV	geom from a fit to **g** tensor values V
∠CFeC					
α_ξ	90.8^e(89.2^d)	90.6		90.9^e(89.1)	91.1
α_η	90.7^e(89.3^d)	91.0		90.8^e(89.2)	91.0
α_ζ	91.1^e(88.9^d)	91.1		90.5^e(89.5)	90.6
Q_ξ	0.054(−0.054)	0.041		0.061(−0.061)	0.077
Q_η	0.047(−0.047)	0.069		0.054(−0.054)	0.069
Q_ζ	0.074(−0.074)	0.076		0.034(−0.034)	0.041
$Q(\alpha_{1g})$	0.101(−0.101)	0.105		0.086(−0.086)	0.105
$Q(\epsilon_g{:}x)$	0.019(−0.019)	0.017		−0.019(0.019)	−0.025
$Q(\epsilon_g{:}y)$	0.005(−0.005)	−0.019		0.005(−0.005)	0.005
g Tensor					
g_1	1.053(1.413)	0.994	0.915	1.186(1.462)	0.994
g_2	2.193(1.642)	2.179	2.100	2.139(1.702)	2.180
g_3	2.376(2.597)	2.429	2.350	2.332(2.512)	2.429
SD[a]	0.084(0.360)	0.068		0.137(0.348)	0.069
Trigonal Orbital Splittings					
a_1	120(−126)	128	$e(xy) = 25$	103(−108)	129
e	−42, −78(48,78)	−39, −89	$e(yz) = -99$ $e(xz) = 65$	−33,−70(38,70)	−39, −90

(b) Directional Cosines

	II			III			V		
axis	g_1	g_2	g_3	g_1	g_2	g_3	g_1	g_2	g_3
	0.994	2.179	2.429	0.915	2.100	2.350	0.991	2.181	2.430
x	0.630	−0.059	−0.774	0.002	0.573	−0.819	0.535	0.759	−0.371
y	0.561	−0.655	0.506	0.710	0.567	0.418	0.563	−0.648	−0.514
z	0.537	0.754	0.379	−0.694	0.581	0.423	0.630	−0.066	0.774
a	0.981	0.031	0.250	0.000	0.500	0.866	0.988	−0.147	0.005
b	0.255	−0.075	−0.956	0.000	0.866	0.500	0.142	0.896	−0.404
c	−0.007	0.990	−0.084	1.000	0.000	0.000	0.058	0.404	0.906

[a] Legend: SD, standard deviation between calculated and experimental *g* values; $k = 0.79$; $\zeta = 345$ cm^{-1}; $B = 720$; $C = 3290$ cm^{-1}. [b] Crystallographic axes: $a = 13.422$ Å; $b = 10.399$ Å; $c = 8.381$ Å (*Pnca* space group). [c] Pseudo orthorhombic. [d] Angles along the approximate C_3 direction running nearly parallel to the crystallographic *a* axis; the other angles (cis to the listed ones) are 90.88, 90.87, 92.02, 90.87, 90.90, and 89.54. [e] Adopted from the reported bond angles α after changing the sign of (α − 90°) from negative to positive (see text).

vibronic state and a Γ_8 state at higher energy. The **g** tensor of the ground vibronic state Γ_7 is given by

$$\mathbf{g}(\Gamma_7) = \frac{1}{3}(2 + 4k) \tag{42}$$

The orbital reduction factor *k* can be expressed as

$$k = k_{\text{cov}} \cdot k_{\text{CI}} \cdot [K_{T_2}(T_1)] \tag{43}$$

k_{cov} is the covalent reduction factor, k_{CI} arises from configurational mixing between the Γ_7 ($^2T_{2g}(t_{2g}{}^5)$) ground state and all other excited states of the same symmetry.[51] $K_{T_2}(T_1)$ is the vibronic (Ham) reduction factor, which includes all information about the vibronic nature of the Γ_7 ground state.[52] Approximate expressions for these factors as a function of the strength of the $^2T_{2g} \otimes \tau_{2g}$ JT coupling have been reported.[32,53−55] In the usual treatment of the dynamic JT effect, one assumes that vibronic coupling is stronger than spin−orbit coupling, and the latter is modified according to $K_{T_2}(T_1)$. In Figure 14 the lowest vibronic levels and $K_{T_2}(T_1)$ are plotted vs the vibronic coupling strength λ_τ. Small values of λ_τ (weak vibronic coupling) lead already to a strong reduction of the $^2A_{1g}$−$^2T_{2g}$ energy gap and of $K_{T_2}(T_1)$ (δ is the tunneling splitting in the strong vibronic coupling limit). For octahedral $[Fe(CN)_6]^{3-}$ and with neglect of influences from spin−orbit coupling and strain $\lambda_\tau = 0.965$ (Table 5), δ drops from its initial value ($\delta = \hbar\omega_\tau = 93$ cm^{-1}) to 30 cm^{-1}, accompanied by a nearly total quenching of *k* ($K_{T_2}(T_1) = 0.138$). The situation drastically changes when dynamic Jahn−Teller coupling and spin−orbit coupling are accounted for on the same footing. This should be done because the two effects are comparable in magnitude (see section IVc). In this case δ is equal to the energy difference between the first excited state Γ_8 and the ground-state vibronic level Γ_7 (Figure 14a), i.e., 70 cm^{-1}, in comparison to its nominal value of 93 cm^{-1}. In line with this, the vibronic reduction for $[Fe(CN)_6]^{3-}$ remains only 12% ($K_{T_2}(T_1) = 0.876$; see Figure 14b), therefore leaving the value of *g* only weakly affected by vibronic coupling ($g(\Gamma_7) = 1.835$), in comparison to the static octahedral limit ($g(\Gamma_7) = 1.918$).

We now discuss the combined effect of geometric strain and dynamic JT coupling. In Figure 15 are presented the λ_τ dependence of the magnetic susceptibility ($\Delta\chi_i$, i = *a*, *b*, *c*; *T* = 5 K) and the **g** tensor ($\mathbf{g}_i$) for the vibronic ground state of $[Fe(CN)_6]^{3-}$ in its monoclinic form (set V in Table 9). In these

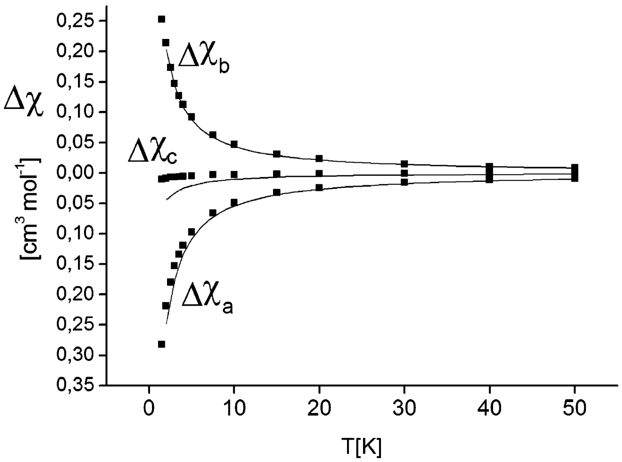

Figure 13. Experimental (black squares)[21] and theoretical anisotropic magnetic susceptibilities for $[Fe(CN)_6]^{3-}$. The notations $\Delta\chi_a$, $\Delta\chi_b$, and $\Delta\chi_c$ are defined as $\Delta\chi_a = \chi_1 - \chi_3$, $\Delta\chi_b = \chi_2 - \chi_1$, and $\Delta\chi_c = \chi_2 - \chi_3$. χ_1, χ_2, and χ_3 are the principal crystal susceptibilities with orientations along the *a*, *b*, and *c* crystallographic axes, respectively; these coincide (within an angle of ±5°) with the (1,1,1), (2,−1,−1), and (0,1,−1) D_{3d} directions of the $[Fe(CN)_6]^{3-}$ complex (in the coordinate system *x*, *y*, *z*, defined by the Fe−C bond vectors) and with principal axes of the molecular **g** tensor 0.915, 2.100, and 2.350 ($T = 12$ K[13]), respectively. The following set of ligand field parameters describing the effect due to the geometrical strain (in cm^{-1}) have been used (set V, Table 9, in combination with eq 21): $\langle xy|V_{LF}|xy\rangle = -3$, $\langle xy|V_{LF}|yz\rangle = 70$, $\langle yz|V_{LF}|yz\rangle = 2$, $\langle xz|V_{LF}|xy\rangle = 79$, $\langle yz|V_{LF}|xz\rangle = 41$, $\langle xz|V_{LF}|xz\rangle = 1$; $\langle x^2 - y^2|V_{LF}|x^2 - y^2\rangle = \langle z^2|V_{LF}|z^2\rangle = 34950$; $B = 720$, $C = 3290$; $\zeta = 345$ cm^{-1}; $k = 0.79$.

calculations, we have assumed that the energy of the τ_{2g} mode ($\hbar\omega_\tau = 93$ cm^{-1}) remains unchanged, when the free $[Fe(CN)_6]^{3-}$ complex is embedded in its crystal surrounding. In contrast to $\Delta\chi_i$, which is not found to be sensitive to λ_τ, $\mathbf{g}_i$ shows a clear dependence on λ_τ, particularly pronounced for the smaller component g_1. When λ_τ increases, starting from the static strain induced geometry, there is a strong reduction of g_1 from its initial value (0.994; Table 9, set V) to 0.197. Apparently, there is an enhancement of the geometric strain by dynamic JT coupling. We also calculate a clear temperature effect on all **g** tensor values; the smaller component g_1 increases (by 20%), while the larger g_2 and g_3 values decrease (by 4% and 3%, respectively), when the temperature (T) is increased from 0 to 50 K. That is, the increase of the temperature counteracts the changes induced by the dynamic JT effect. The calculated strain induced changes of the **g** tensor are comparable with those reported (both experimental and calculated) for other strain-affected dynamic JT coupling systems, such as CuF_6^{2-},[56] $Cu(H_2O)_6^{2+}$,[57] (including temperature dependencies for both, see ref 58), $TiCl_6^{3-}$,[59] and aqua complexes of Ti^{III} (t_{2g}^1)[60−63] and V^{III} (t_{2g}^2).[64,65] When we compare the results presented here with the **g** tensor values of $[Fe(CN)_6]^{3-}$from experiment (Table 9), we conclude that dynamic JT coupling is prohibited in the $K_3Fe(CN)_6$ crystal lattice. However, the results obtained may stimulate further experiments on this and other related systems, such as $Cs_2KFe(CN)_6$, for which temperature-dependent structural and EPR data are still missing.[66]

c. Near-IR Spectra and the Anisotropic Susceptibility of $K_3[Mn(CN)_6]$. Potassium hexacyanomanganate(III) is isomorphic with the corresponding cobalt salt. Unfortunately, the structures of neither of the two compounds are known with good accuracy (see Table 8). Single-crystal susceptibilities of $K_3[Mn(CN)_6]$ have been reported, and a distinct anisotropy between 80 and 300 K has been found.[24] To interpret these data, a crystal field model with tetragonal D_{4h} symmetry has been adopted.[24]

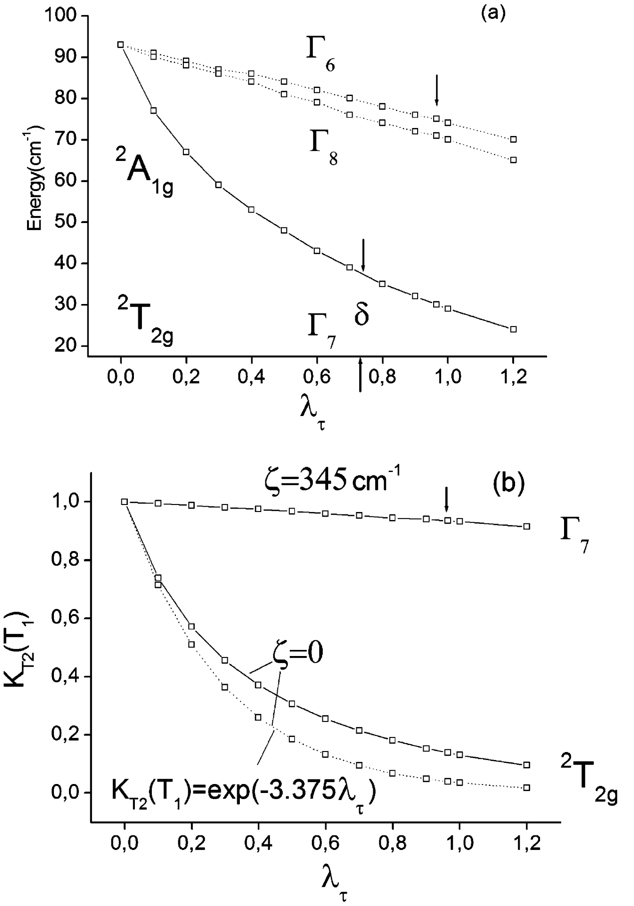

Figure 14. (a) Energies (cm^{-1}) of the lowest vibronic states of $[Fe(CN)_6]^{3-}$ without ($^2T_{2g}$ and $^2A_{1g}$) and with (Γ_7, Γ_8, Γ_6) spin−orbit coupling. The lowest vibronic state ($^2T_{2g}$ or Γ_7) has been taken as an energy reference; the tunneling splitting δ of the fourfold degenerate vibronic state (strong vibronic coupling limit) is indicated. (b) Vibronic (Ham) reduction factors $K_{T_2}(T_1)$ for the angular momentum operator ($\mathbf{L}(T_1)$) in the ground vibronic state of $[Fe(CN)_6]^{3-}$. The vertical arrows mark the value of λ_τ for $[Fe(CN)_6]^{3-}$ (see Table 5). Solid lines are obtained with a full diagonalization of the vibronic Hamiltonian; dotted lines correspond to the expression obtained with perturbation theory.[53]

The electronic spectrum of $K_3[Mn(CN)_6]$ has been reported.[22,23,41] Two sharp transitions at 9216 and 9461 cm^{-1} with polarizations ⊥ and || to the crystal axis (the needle axis) have been observed.[22] The former was reproduced in a later study[25] and assigned to the $^3T_{1g} \rightarrow {}^1T_{2g}$ spin-flip transition within the t_{2g}^4 ground-state configuration of $[Mn(CN)_6]^{3-}$. Electronic absorption spectra in the region of the 9191 cm^{-1} transition at different temperatures are represented in Figure 16. With an increase of temperature two hot bands (at 9116 and 9012 cm^{-1}) appear in the spectrum above 11 K. The first is located at 75 cm^{-1} lower energy; it is quite sharp at 25 K, and it is very probably the second electronic origin from the spin−orbit/ligand field split $^3T_{1g}$ ground-state multiplet. It has a comparatively intense sideband at 339 cm^{-1} higher energy, which corresponds to the frequency of the t_{1u} vibration already observed as a vibronic sideband of the first origin. At still higher temperatures, the spectrum quickly becomes broadened but a third hot band at about 181 cm^{-1} grows in. We can tentatively assign this to a third component of the ground state. Note that the ratio of the two energies 181/75 = 2.41 does not obey the Landé interval rule, which implies a ratio of 3 if the three transitions were to be interpreted as originating solely from splitting of the $^3T_{1g}$ ground term, due to spin−orbit coupling. In analogy to $K_3[Fe(CN)_6]$, we can assume that $[Mn(CN)_6]^{3-}$ is trigonally

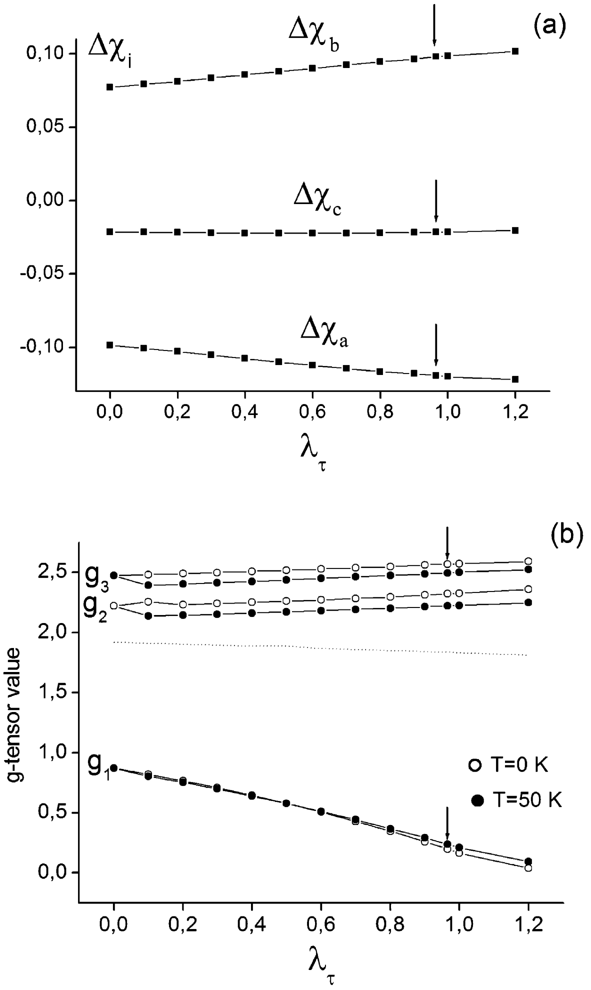

Figure 15. Effect of dynamic JT coupling (linear $^2T_{2g}\otimes\tau_{2g}$ model) on the anisotropic susceptibilities (a; T = 5 K) and **g** tensors (b) of $[Fe(CN)_6]^{3-}$ in dependence of the vibronic coupling strength (λ_τ) in the presence of geometric strain. Values of the strain energies as well as other parameters taken in the calculation are specified in Table 9 (set V). The dotted curve in (b) refers to octahedral $[Fe(CN)_6]^{3-}$, calculated when excluding the strain. The vertical arrows mark the value of λ_τ for $[Fe(CN)_6]^{3-}$ (see Table 5).

elongated (the compounds are isomorphic). On the basis of the anisotropy of the susceptibility tensor, an axial compression can be ruled out.[24] We can use the observed ground-state splitting to fit the spin−orbit coupling constant and the angle θ (all other parameters, specified in Table 7, have been taken as fixed). Results from this calculation are given in Table 10. A value of $\Delta\theta$ of only $-0.44°$ along with $\zeta = 209$ cm^{-1} can readily account for the experimental results. With these parameters, energies of excited states, split from $^1T_{2g}$, are calculated in agreement with experiment, and they are consistent with the reported polarizations (Table 10). Finally, a set of all these parameters has been used to calculate the susceptibility tensor; the calculated and experimental data are compared in Figure 17. There is excellent agreement between theory and experiment. We therefore conclude that a trigonally elongated geometry (as in $[Fe(CN)_6]^{3-}$ with an orbitally nondegenerate ground state) is compatible with the spectroscopic and magnetic behavior of $[Mn(CN)_6]^{3-}$. As with $[Fe(CN)_6]^{3-}$, the magnetic anisotropy is found to be extremely sensitive with respect to angular distortions.

VII. Conclusions

(1) JT coupling in hexacyanometalates with degenerate $^2T_{2g}$ and $^3T_{1g}$ ground states ($T_g\otimes(\epsilon_g+\tau_{2g})$ coupling) is usually neglected, because it is a weak effect due to π-bonding. However, π-bonding is also responsible for the magnetic properties due to exchange coupling in room-temperature and single-molecule magnets. Since both effects are comparable in magnitude, they need to be accounted for on the same footing when spectroscopic and magnetic properties are modeled and interpreted.

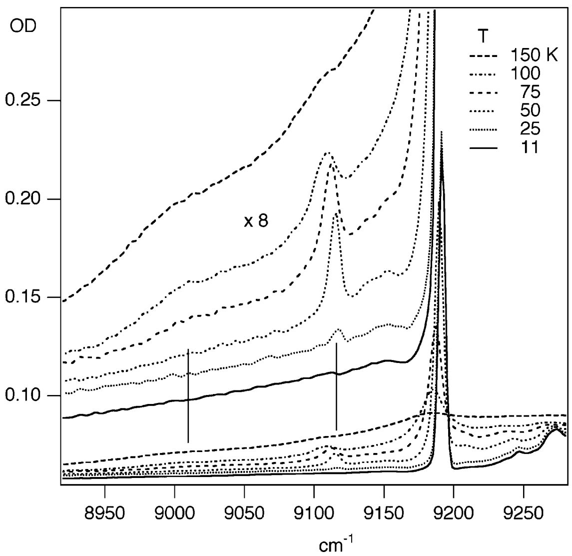

Figure 16. Near-IR spectra in high resolution for $[Mn(CN)_6]^{3-}$ in the region of the $^3T_{1g}-{}^1T_{2g}$ transition with hot bands which grow upon an increase of temperature.

TABLE 10: Energies of the Lowest Electronic States[a] Involved in the Spectroscopy and Magnetism of $[Mn(CN)_6]^{3-}$

						exptl	
O_h, $\zeta = 0$		D_{3d}, $\zeta = 0$		D_{3d},[d] $\zeta = 209$		b	c
$^3T_{1g}$	0	$^3A_{2g}$	0	A_{1g} [A_{1g}]	0	0	
		^3E_g	159	E_g [T_{1g}]	75	75	
				A_{2g} [T_{1g}]	181	181	
				A_{1g} [T_{2g},E_g]	296		
				E_g [T_{2g},E_g]	331		
				E_g [T_{2g},E_g]	386		
$^1T_{2g}$	9096	^1E_g	9123	E_g [T_{2g}]	9250	9191	9216 (⊥)[e]
		$^1A_{1g}$	9335	A_{1g} [T_{2g}]	9462	9390	9461 (‖)[e]

[a] ζ = 209 cm^{-1} and θ = 54.29° calculated from a fit to the experimental energies of the $A_{1g}\rightarrow E_g$ (75 cm^{-1}) and $A_{1g}\rightarrow A_{2g}$ (181 cm^{-1}) transitions within the $^3T_{1g}$ octahedral ground state. Other parameters are B = 675, C = 3120 cm^{-1}, $10Dq$ = 34 000 cm^{-1}, e_σ = 8976 cm^{-1}, and e_π = −1783 cm^{-1} (see Table 7). The D_{3d} trigonal splitting of the t_{2g} orbitals into $a_{1g} < e_g$ is 110 cm^{-1}. [b] This work. [c] Reference 22. [d] The origin from the corresponding term in the O_h double group is given in brackets. [e] Polarization with electric vector E perpendicular (⊥) or parallel (‖) to the crystal axis taken to coincide with the needle axis of the dark red crystals.

(2) We present a simple method, which allows us to determine all parameters of the $T_g\otimes(\epsilon_g+\tau_{2g})$ JT problem with DFT calculations. First- and second-order vibronic coupling constants can be used to calculate the depth and position of stationary points of D_{4h}, D_{3d}, and D_{2h} symmetry on the ground-state potential energy surface and also to assign them to minima and saddle points of different order. There is no way to get the same information from DFT alone, because present implementations of Kohn−Sham DFT do not allow calculations of the energy of the system in the case of orbitally degenerate ground states. In addition, technical problems occur when a scan of the potential energy surface is attempted point by point in low symmetry, where electrons jump between orbitals which are

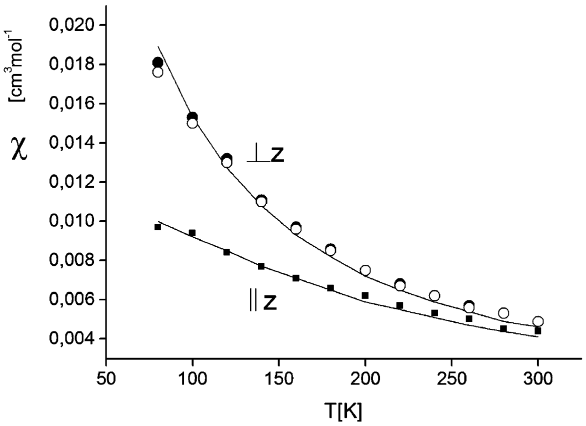

Figure 17. Experimental (black squares, open and full circles)[24] and calculated (solid line, JT coupling model, trigonal distortion of $\theta = 54.29°$; see Table 10 for a full list of parameters used) anisotropic magnetic susceptibilities of $[\mathrm{Mn(CN)_6}]^{3-}$. The direction *z* is parallel to the trigonal C_3 axis and coincides (within 5°) with the crystallographic (*a*) direction; the molecular *x* and *y* axes (represented here by full and open circles, respectively) deviate by only 13 and 7° from the crystallographic (*b*) and (*c*) axes.

different in space but close in energy, and this makes it difficult to define proper electronic configurations.

(3) When spin−orbit coupling is neglected, we find that D_{3d}-distorted structures represent absolute minima in the case of $\mathrm{M(CN)_6}$ (M = $\mathrm{Fe^{III}}$, $\mathrm{Mn^{III}}$, $\mathrm{Cr^{II}}$, $\mathrm{Mn^{II}}$), while $[\mathrm{Ti(CN)_6}]^{3-}$ is tetragonal (D_{4h}). A remarkable trend with a correlation between JT coupling and metal−ligand π-back-donation is found: $\mathrm{Ti^{III}} < \mathrm{V^{III}} < \mathrm{Mn^{III}} < \mathrm{Fe^{III}} < \mathrm{Mn^{II}} < \mathrm{Cr^{II}}$.

(4) On the basis of a comparison between the vibronic coupling strengths (i.e., the ratios of the JT stabilization energy (E_{JT}) and the zero point vibrational energy; $\lambda_\epsilon = E_{\mathrm{JT}}(D_{4h})/\hbar\omega_\epsilon$ ($\mathrm{T_g}\otimes\epsilon_{\mathrm{g}}$ coupling), $\lambda_\tau = 2E_{\mathrm{JT}}(D_{4h})/3\hbar\omega_\tau$ ($\mathrm{T_g}\otimes\tau_{2\mathrm{g}}$ coupling)) it is found that JT coupling with the $\tau_{2\mathrm{g}}$ mode is strong for $\mathrm{Cr^{II}}$ and $\mathrm{Mn^{II}}$, moderate for $\mathrm{Mn^{III}}$ and $\mathrm{Fe^{III}}$, and weak in all other cases.

(5) The interplay between JT coupling and spin−orbit coupling is found to lead to a shallow D_{3d} minimum for $[\mathrm{Fe(CN)_6}]^{3-}$ and no distortion for $[\mathrm{Mn(CN)_6}]^{3-}$. However, the ground-state potential energy surfaces of both ions are found to be flat and susceptible to angular distortions. Therefore, we have been able to reproduce the **g** and magnetic susceptibility tensors of $\mathrm{K_3[Fe(CN)_6]}$ and the spectra and susceptibility tensor of $\mathrm{K_3[Mn(CN)_6]}$ in terms of statically distorted and strain-induced geometries (geometrical strains) and a small trigonal distortion (trigonal strains of only 1 and 0.5°, respectively).

(6) Pseudo JT coupling, due to mixing of the $\mathrm{t_{2g}}$ and $\mathrm{e_g}$ orbitals via the $\tau_{2\mathrm{g}}$ vibrational mode, is found to be of minor importance for $[\mathrm{Fe(CN)_6}]^{3-}$ and possibly also for the other complexes discussed. The reason is the rather high value of the cubic ligand field spitting due to the cyanide ligands, which leads to a partial or a complete suppression of the $\mathrm{t_{2g}}\otimes\tau_{2\mathrm{g}}\otimes\epsilon_{\mathrm{g}}$ pseudo JT interaction, in contrast to the case for tetrahedral complexes.[33]

(7) Dynamic JT coupling in addition to the structural strain is found in solids and produces interesting effects on the **g** tensor values and to a lesser extent on the magnetic susceptibilities with JT active $\mathrm{E_g}$ or $\mathrm{T_g}$ ground states.[56−65] These deserve further experimental studies.

Appendix

With eqs 10−14 we obtain the following master equations, which relate the parameters of the vibronic coupling Hamiltonian equation (1) with quantities calculated from DFT.

(a) From data based on D_{4h} geometry optimizations (to get Q_θ^{m} and Q_θ^{s}) and a single-point calculation (to get $E_{\mathrm{FC}}^{\mathrm{m}}(D_{4h})$):

$$V_\epsilon = \frac{4}{4 - r_\epsilon}\cdot\frac{E_{\mathrm{FC}}^{\mathrm{m}}(D_{4h})}{Q_\theta^{\mathrm{m}}} \tag{A.1}$$

$$K_\epsilon = \frac{1 - r_\epsilon}{4 - r_\epsilon}\cdot\frac{4}{3}\cdot\frac{E_{\mathrm{FC}}^{\mathrm{m}}(D_{4h})}{(Q_\theta^{\mathrm{m}})^2} \tag{A.2}$$

$$L_\epsilon = \frac{2 + r_\epsilon}{4 - r_\epsilon}\cdot\frac{4}{3}\cdot\frac{E_{\mathrm{FC}}^{\mathrm{m}}(D_{4h})}{(Q_\theta^{\mathrm{m}})^2} \tag{A.3}$$

where $r_\epsilon = Q_\theta^{\mathrm{m}}/Q_\theta^{\mathrm{s}}$.

(b) From structural data based on D_{3d} geometry optimizations (to get Q_τ^{m} and Q_τ^{s}) and a single-point calculation (to get $E_{\mathrm{FC}}^{\mathrm{m}}(D_{3d})$):

$$V_\tau = -\frac{2}{r_\tau - 4}\cdot\frac{E_{\mathrm{FC}}^{\mathrm{m}}(D_{3d})}{Q_\tau^{\mathrm{m}}} \tag{A.4}$$

$$K_\tau = \frac{r_\tau - 1}{r_\tau - 4}\cdot\frac{4}{9}\cdot\frac{E_{\mathrm{FC}}^{\mathrm{m}}(D_{3d})}{(Q_\tau^{\mathrm{m}})^2} \tag{A.5}$$

$$X_\tau = \frac{r_\tau + 2}{r_\tau - 4}\cdot\frac{1}{3}\cdot\frac{E_{\mathrm{FC}}^{\mathrm{m}}(D_{3d})}{(Q_\tau^{\mathrm{m}})^2} \tag{A.6}$$

where $r_\tau = Q_\tau^{\mathrm{m}}/Q_\tau^{\mathrm{s}}$.

(c) From structural data based on D_{2h} optimization (to get Q_ζ^{m} and $Q_\theta^{\mathrm{m}'}$):

$$W = \frac{V_\epsilon + (2K_\epsilon - L_\epsilon)Q_\theta^{\mathrm{m}'}}{2Q_\varsigma^{\mathrm{m}}} \tag{A.7}$$

$$L_\tau = 2K_\tau - 2\,\frac{V_\tau}{Q_\varsigma^{\mathrm{m}}} - \frac{V_\epsilon Q_\theta^{\mathrm{m}'}}{(Q_\varsigma^{\mathrm{m}})^2} - \frac{(2K_\epsilon - L_\epsilon)(Q_\theta^{\mathrm{m}'})^2}{(Q_\varsigma^{\mathrm{m}})^2} \tag{A.8}$$

Substitution of V_ϵ, K_ϵ, L_ϵ, and V_τ with expressions A.1−A.4 yields

$$W = \frac{2E_{\mathrm{FC}}^{\mathrm{m}}(D_{4h})}{Q_\varsigma^{\mathrm{m}}Q_\theta^{\mathrm{m}}}\,\frac{1 - r_\epsilon\dfrac{Q_\theta^{\mathrm{m}'}}{Q_\theta^{\mathrm{m}}}}{4 - r_\epsilon} \tag{A.9}$$

$$L_\tau = \frac{4E_{\mathrm{FC}}^{\mathrm{m}}(D_{3d})}{(r_\tau - 4)Q_\tau^{\mathrm{m}}}\left[\frac{2}{9}\,\frac{(r_\tau - 1)}{Q_\tau^{\mathrm{m}}} + \frac{1}{Q_\varsigma^{\mathrm{m}}}\right] - \frac{4E_{\mathrm{FC}}^{\mathrm{m}}(D_{4h})}{(4 - r_\epsilon)}\left[\frac{Q_\theta^{\mathrm{m}'}}{(Q_\varsigma^{\mathrm{m}})^2 Q_\theta^{\mathrm{m}}} - r_\epsilon\left(\frac{Q_\theta^{\mathrm{m}'}}{Q_\theta^{\mathrm{m}}Q_\varsigma^{\mathrm{m}}}\right)^2\right] \tag{A.10}$$

We obtain the following equations for the energies of the Franck−Condon transitions:

$$E_{\mathrm{FC}}^{\mathrm{m}}(D_{2h}, \mathrm{b_{2g}} \rightarrow \mathrm{b_{3g}}) = 2V_\tau Q_\varsigma^{\mathrm{m}} + 2WQ_\varsigma^{\mathrm{m}}Q_\theta^{\mathrm{m}'} \tag{A.11}$$

$$E_{\mathrm{FC}}{}^{\mathrm{m}}(D_{2h}, \mathrm{b}_{2\mathrm{g}} \rightarrow \mathrm{a}_{\mathrm{g}}) = -\frac{3}{2}\left(V_{\epsilon} Q_{\theta}{}^{\mathrm{m}'} - \frac{1}{2} L_{\epsilon}(Q_{\theta}{}^{\mathrm{m}'})^2 - \frac{1}{2} L_{\tau}(Q_{\varsigma}{}^{\mathrm{m}})^2\right) + V_{\tau} Q_{\varsigma}{}^{\mathrm{m}} + W Q_{\varsigma}{}^{\mathrm{m}} Q_{\theta}{}^{\mathrm{m}'} \quad (\mathrm{A}.12)$$

and expressed in terms of quantities derived from DFT:

$$E_{\mathrm{FC}}{}^{\mathrm{m}}(D_{2h}, \mathrm{b}_{2\mathrm{g}} \rightarrow \mathrm{b}_{3\mathrm{g}}) = \frac{4E_{\mathrm{FC}}{}^{\mathrm{m}}(D_{3d})}{4 - r_{\tau}} \frac{Q_{\varsigma}{}^{\mathrm{m}}}{Q_{\tau}{}^{\mathrm{m}}} + \frac{4E_{\mathrm{FC}}{}^{\mathrm{m}}(D_{4h})}{4 - r_{\epsilon}} \frac{Q_{\theta}{}^{\mathrm{m}'}}{Q_{\theta}{}^{\mathrm{m}}} \left(1 - r_{\epsilon} \frac{Q_{\theta}{}^{\mathrm{m}'}}{Q_{\theta}{}^{\mathrm{m}}}\right) \quad (\mathrm{A}.13)$$

$$E_{\mathrm{FC}}{}^{\mathrm{m}}(D_{2h}, \mathrm{b}_{2\mathrm{g}} \rightarrow \mathrm{a}_{\mathrm{g}}) = \frac{E_{\mathrm{FC}}{}^{\mathrm{m}}(D_{3d})}{r_{\tau} - 4} \frac{Q_{\varsigma}{}^{\mathrm{m}}}{Q_{\tau}{}^{\mathrm{m}}} \left[1 + \frac{2}{3}(r_{\tau} - 1) \frac{Q_{\varsigma}{}^{\mathrm{m}}}{Q_{\tau}{}^{\mathrm{m}}}\right] + \frac{E_{\mathrm{FC}}{}^{\mathrm{m}}(D_{4h})}{4 - r_{\epsilon}} \frac{Q_{\theta}{}^{\mathrm{m}'}}{Q_{\theta}{}^{\mathrm{m}}} \left[-7 + 2(1 + r_{\epsilon}) \frac{Q_{\theta}{}^{\mathrm{m}'}}{Q_{\theta}{}^{\mathrm{m}}}\right] \quad (\mathrm{A}.14)$$

In the case of linear JT coupling we have

$$Q_{\theta}{}^{\mathrm{m}} = \frac{V_{\epsilon}}{K_{\epsilon}}$$

$$Q_{\theta}{}^{\mathrm{m}'} = -\frac{1}{2}\frac{V_{\epsilon}}{K_{\epsilon}}$$

$$Q_{\tau}{}^{\mathrm{m}} = \frac{2}{3}\frac{V_{\tau}}{K_{\tau}}$$

$$Q_{\varsigma}{}^{\mathrm{m}} = \frac{V_{\tau}}{K_{\tau}}$$

and therefore obtain

$$\frac{Q_{\theta}{}^{\mathrm{m}'}}{Q_{\theta}{}^{\mathrm{m}}} = -\frac{1}{2}$$

$$\frac{Q_{\varsigma}{}^{\mathrm{m}}}{Q_{\tau}{}^{\mathrm{m}}} = \frac{3}{2}$$

$$r_{\epsilon} = \frac{Q_{\theta}{}^{\mathrm{m}}}{Q_{\theta}{}^{\mathrm{s}}} = -2$$

$$r_{\tau} = \frac{Q_{\tau}{}^{\mathrm{m}}}{Q_{\tau}{}^{\mathrm{s}}} = -2$$

Substitution into eqs A.13 and A.14 yields

$$E_{\mathrm{FC}}{}^{\mathrm{m}}(D_{2h}, \mathrm{b}_{2\mathrm{g}} \rightarrow \mathrm{b}_{3\mathrm{g}}) = E_{\mathrm{FC}}{}^{\mathrm{m}}(D_{3d})$$

$$E_{\mathrm{FC}}{}^{\mathrm{m}}(D_{2h}, \mathrm{b}_{2\mathrm{g}} \rightarrow \mathrm{a}_{\mathrm{g}}) = \frac{1}{2}\left[E_{\mathrm{FC}}{}^{\mathrm{m}}(D_{4h}) + E_{\mathrm{FC}}{}^{\mathrm{m}}(D_{3d})\right]$$

as given in Table 2.

Acknowledgment. This study was performed within the priority program SPP 1137 (Molecular Magnetism) of the German Scientific Foundation (DFG). We are grateful for fruitful discussions with various colleagues at the International Symposium of the Jahn−Teller Effect, Trieste, Italy, 2006. Thanks are also due to Prof. D. Reinen (University of Marburg, Germany) for discussions in the course of this work as well as for careful reading of the manuscript prior to publication.

Supporting Information Available: Text and tables giving computational details and additional derivations mentioned in the text. This material is available free of charge via the Internet at http://pubs.acs.org.

References and Notes

(1) Teller, E. A historical note. In *The Jahn-Teller Effect in Molecules and Crystals*; Engelman, R., Ed.; Wiley-Interscience: London, 1972.

(2) Jahn, H. A.; Teller, E. *Proc. R. Soc. London, Ser. A* **1937**, *161*, 220.

(3) Ruiz, E.; Rodriguez-Fortea, A.; Alvarez, S.; Verdaguer, M. *Chem. Eur. J.* **2005**, *11*, 2135.

(4) Atanasov, M.; Comba, P.; Daul, C. A. *J. Phys. Chem. A* **2006**, *110*, 13332.

(5) Reinen, D.; Friebel, C. *Struct. Bonding* **1979**, *37*, 1.

(6) Halcrow, M. A. *Dalton Trans.* **2003**, 4375.

(7) Reinen, D.; Atanasov, M. *Magn. Reson. Rev.* **1991**, *15*, 167.

(8) Bersuker, I. B.; Polinger, V. Z. *Phys. Lett.* **1973**, *44A*, 495.

(9) Bacci, M.; Ranfagni, A.; Fontana, M. P.; Viliani, G. *Phys. Rev. B* **1975**, *11*, 3052.

(10) Bacci, M.; Ranfagni, A.; Cetica, M.; Viliani, G. *Phys. Rev. B* **1975**, *12*, 5907.

(11) Atanasov, M.; Comba, P. *J. Mol. Struct.* **2007**, 838, 157.

(12) Ceulemans, A.; Beyens, D.; Vanquickenborne, L. G. *J. Am. Chem. Soc.* **1984**, *106*, 5824.

(13) Baker, J. M.; Bleaney, B.; Bowers, K. D. *Proc. Phys. Soc. London, Sect. B* **1956**, *69*, 1205.

(14) Bleaney, B.; O’Brien, M. C. M. *Proc. Phys. Soc. London, Sect. B* **1956**, *69*, 1216.

(15) Figgis, B. N. *Trans. Faraday Soc.* **1961**, *57*, 204.

(16) Golding, R. M. *Mol. Phys.* **1967**, *12*, 13.

(17) Oosterhuis, W. T.; Lang, G. *Phys. Rev.* **1969**, *178*, 439.

(18) Figgis, B. N.; Gerloch, M.; Mason, R. *Proc. R. Soc. London, Ser. A* **1969**, *309*, 91.

(19) Merrithew, P. B.; Modestino, A. J. *J. Am. Chem. Soc.* **1972**, *94*, 3361.

(20) Figgis, B. N.; Skelton, B. W.; White, A. H. *Aust. J. Chem.* **1978**, *31*, 1195.

(21) Baker, J.; Figgis, B. N. *Aust. J. Chem.* **1982**, *35*, 265.

(22) Jones, G. D.; Runciman, W. A. *Proc. Phys. Soc. (London)* **1960**, *76*, 996.

(23) Mukhrjee, R. K.; Chowdhury, M. *Chem. Phys. Lett.* **1975**, *34*, 178.

(24) Ghosh, D.; Mukhrjee, R. K. *J. Phys. Chem. Solids* **1979**, *40*, 691.

(25) Daul, C. A.; Rauzy, C.; Decurtins, S.; Franz, P.; Hauser, A. *Int. J. Quant. Chem.* **2005**, *101*, 753.

(26) Bersuker, I. B. *The Jahn-Teller Effect and Vibronic Interactions in Modern Chemistry*; Plenum Press: New York, 1984.

(27) Bersuker, I. B. *The Jahn-Teller Effect*; Cambridge University Press: London, 2006.

(28) Griffith, J. S. *The Theory of Transition-Metal Ions*; Cambridge University Press: London, 1971.

(29) Öpik, U.; Pryce, M. H. L. *Proc. R. Soc. London, Ser. A* **1957**, *238*, 425.

(30) Atanasov, M.; Daul, C. A. *Chimia* **2005**, *59*, 504.

(31) Reinen, D.; Atanasov, M.; Massa, W. *Z. Anorg. Allg. Chem.* **2006**, *632*, 1375.

(32) Q_{i}' are dimensionless normal coordinates, calculated from Q_{i} (in Å) as $Q_{\mathrm{i}}' = fQ_{\mathrm{i}}$: $f = 0.1722[M(\hbar\omega_{\tau})]^{1/2}$, where M is the reduced mass of the τ_{2g} vibration $M = R_{\mathrm{tr}}{}^{2}\cdot(m_{\mathrm{C}} + m_{\mathrm{N}})/4$, with m_{C} (=12) and m_{N} (=14) in au, $\hbar\omega_{\tau}$ is the vibrational frequency (in cm^{-1}), R_{tr} is the metal−ligand bond distance (in Å). Accordingly, when the vibronic matrix elements are calculated, using the harmonic oscillator wavefunctions ($\langle n - 1|Q_{\tau}'|n\rangle = (n/2)^{1/2}$; $\langle n|Q_{\tau}'|n + 1\rangle = [(n + 1)/2]^{1/2}$), $V_{\tau}Q_{\tau}$ has to be replaced by $V_{\tau}'Q_{\tau}'$ ($V_{\tau}'(\mathrm{cm}^{-1}) = V_{\tau}(\mathrm{cm}^{-1}/\text{Å})/f$, which is the same as $V_{\tau}' = \sqrt{(3/2)E_{\mathrm{JT}}{}^{D_{3d}}\hbar\omega_{\tau}} = (3/2)\hbar\omega_{\tau}\sqrt{\lambda_{\tau}}$. One can also show that $\hbar\omega_{\tau} = K_{\tau}/f^2$; a different definition of the vibronic coupling strength $k = V_{\tau}'/\hbar\omega_{\tau} = (3/2)\sqrt{\lambda_{\tau}}$ has been adopted in ref 53, where approximate expressions for $K_{\mathrm{T}_2}(\mathrm{T}_1) \approx \exp[-(3/2)k^2]$ and for the A_1−T_2 tunneling splitting $\delta \approx 0.88k^2 \exp(-0.827k^2)$ (valid for large k values) are given.

(33) Agresti, A.; Ammeter, J. H.; Bacci, M. *J. Chem. Phys.* **1984**, *81*, 1861; **1985**, *82*, 5299.

(34) Atanasov, M.; Reinen, D. *Adv. Quantum Chem.* **2003**, *44*, 355.

(35) Atanasov, M.; Reinen, D. *Inorg. Chem.* **2005**, *44*, 5092.

(36) Bérces, A.; Bo, C.; Boerrigter, P. M.; Cavallo, L.; Chong, D. P.; Deng, L.; Dickson, R. M.; Ellis, D. E.; Fan, L.; Fischer, T. H.; Fonseca Guerra, C.; van Gisbergen, S. J. A.; Groeneveld, J. A.; Gritsenko, O. V.;

Grüning, M.; Harris, F. E.; van den Hoek, P.; Jacobsen, H.; van Kessel, G.; Kootstra, F.; van Lenthe, E.; McCormack, D. A.; Osinga, V. P.; Patchkovskii, S.; Philipsen, P. H. T.; Post, D.; Pye, C. C.; Ravenek, W.; Ros, P.; Schipper, P. R. T.; Schreckenbach, G.; Snijders, J. G.; Sola, M.; Swart, M.; Swerhone, D.; te Velde, G.; Vernooijs, P.; Versluis, L.; Visser, O.; van Wezenbeek, E.; Wiesenekker, G.; Wolff, S. K.; Woo, T. K.; Baerends, E. J.; Autschbach, J.; Ziegler, T. ADF2006.01 SCM; Theoretical Chemistry, Vrije Universiteit, Amsterdam, The Netherlands, 2006.

(37) Vosko, S. H.; Wilk, L.; Nusair, M. *Can. J. Phys.* **1980**, *58*, 1200.

(38) Klamt, A.; Schürmann, G. *J. Chem. Soc., Perkin Trans. 2* **1993**, 799.

(39) Pye, C. C.; Ziegler, T. *Theor. Chim. Acc.* **1999**, *101*, 396.

(40) Lower, J. A.; Fernelius, W. C. *Inorg. Synth.* **1946**, 2, 225.

(41) Alexander, J. J.; Gray, H. B. *J. Am. Chem. Soc.* **1968**, *90*, 4260.

(42) Reinen, D.; Atanasov, M.; Köhler, P. *J. Mol. Struct.* **2007**, *838*, 151.

(43) Bacci, M. *Chem. Phys. Lett.* **1978**, *58*, 537.

(44) Bacci, M. *Chem. Phys.* **1979**, *40*, 237. Because of a different choice for the definition of Q_ξ, Q_η, and Q_ζ (i.e. in terms of C−M−C valence bond changes instead of angular displacements of single atoms) the value of V_τ, expressed by eq 32, is smaller by a factor of 2, in comparison to the expression given in this reference.

(45) Atanasov, M.; Rauzy, C.; Bättig, P.; Daul, C. A. *Int. J. Quantum Chem.* **2005**, *102*, 119.

(46) Atanasov, M.; Baerends, E. J.; Baettig, P.; Bruyndonckx, R.; Daul, C. A.; Rauzy, C.; Zbiri, M. *Chem. Phys. Lett.* **2004**, *399*, 433.

(47) Buschman, W. E.; Liable-Sands, L.; Rheingold, A. L.; Miller, J. S. *Inorg. Chim. Acta* **1999**, *284*, 175.

(48) (a) Vannerberg, N.-G., *Acta Chem. Scand.* **1970**, *A24*, 2335. (b) Vannerberg, N.-G. *Acta Chem. Scand.* **1972**, *A26*, 2863.

(49) Cauzzi, D. A.; Mori, G.; Predieri, G.; Tiripiccio, A.; Cavatorta, F. *Inorg. Chim. Acta* **1993**, *204*, 181.

(50) Ljungström, E. *Acta Chem. Scand.* **1977**, *A31*, 104.

(51) It is remarkable that, in contrast to $k_{\mathrm{cov}} = 0.79$, a value of k_{CI} larger than one ($k_{\mathrm{CI}} = 1.19$) for $[\mathrm{Fe(CN)_6}]^{3-}$ has been calculated using a full CI calculation (i.e., accounting for the total space of the 256 Slater determinants). This yields $k = k_{\mathrm{cov}}k_{\mathrm{CI}} = 0.940$ ($K_{\mathrm{T_2}}(\mathrm{T_1}) = 1$). This might explain the unusual result that a value of $k = 0.913$ was obtained from a fit to magnetic susceptibility data for $[\mathrm{N(PPh_3)_2}]_3[\mathrm{Fe(CN)_6}]$, using static ligand field expressions for cubic symmetry: Atanasov, M.; Comba, P.; Lampeka, Y. D.; Linti, G.; Malcherek, T.; Miletich, R.; Prikhod'ko, A. I. *Chem. Eur. J.* **2006**, *12*, 737.

(52) Ham, F. S. *Phys. Rev.* **1965**, *138*, A1727.

(53) Caner, M.; Englman, R. *J. Chem. Phys.* **1966**, *44*, 4054.

(54) O'Brien, M. C. M. *Phys. Rev.* **1969**, *187*, 407.

(55) Bersuker, I. B.; Polinger, V. Z. *Phys. Status Solidi B* **1973**, *60*, 85.

(56) Riley, M. J.; Hitchman, M. A.; Reinen, D. *Chem. Phys.* **1986**, *102*, 11.

(57) Riley, M. J.; Hitchman, M. A.; Wan Mohammed, A. *J. Chem. Phys.* **1987**, *87*, 3766.

(58) Riley, M. J. *Top. Curr. Chem.* **2001**, *214*, 57.

(59) Ameis, R.; Kremer, S.; Reinen, D. *Inorg. Chem.* **1985**, *24*, 2751.

(60) Dubicki, L.; Riley, M. J. *J. Chem. Phys.* **1997**, *106*, 1669.

(61) Tregenna-Piggott, P. L. W.; O'Brien, M. C. M.; Pilbrow, J. R.; Güdel, H.-U.; Best, S. P.; Noble, C. J. *J. Chem. Phys.* **1997**, *107*, 8275.

(62) Tregenna-Piggott, P. L. W.; Noble, C. J.; Pilbrow, J. R. *J. Chem. Phys.* **2000**, *113*, 3289.

(63) Tregenna-Piggott, P. L. W.; Güdel, H.-U. *Inorg. Chem.* **2001**, *40*, 5497.

(64) Tregenna-Piggott, P. L. W.; Spichiger, D.; Carver, G.; Frey, B.; Meier, R.; Weihe, H.; Cowan, J. A.; McIntyre, G. J.; Zahn, G.; Barra, A.-L. *Inorg. Chem.* **2004**, *43*, 8049.

(65) Tregenna-Piggott, P. L. W.; Carver, G. *Inorg. Chem.* **2004**, *43*, 8061.

(66) Reynolds, P. A.; Delfs, C. D.; Figgis, B. N.; Moubaraki, B.; Murray, K. S. *Aust. J. Chem.* **1992**, *45*, 1301.